Shear deformation theories for elastic buckling of fluid-infiltrated porous plates: An analytical approach

Journal Pre-proofs

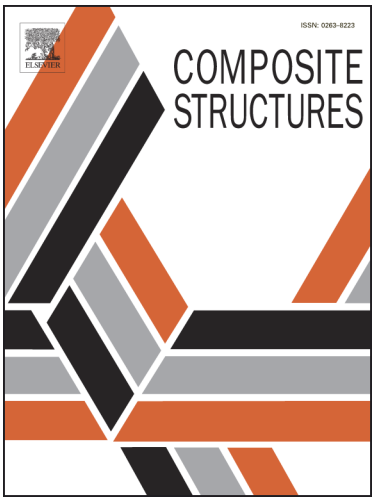

Shear Deformation Theories for Elastic Buckling of Fluid-infiltrated Porous Plates: An Analytical Approach

E. Sadeghi Rad, A.R. Saidi, A.S. Rezaei, M. Askari

PII: S0263-8223(20)32755-0
DOI: https://doi.org/10.1016/j.compstruct.2020.112829
Reference: COST 112829

To appear in: *Composite Structures*

Received Date: 11 June 2020
Revised Date: 1 August 2020
Accepted Date: 10 August 2020

Please cite this article as: Rad, E.S., Saidi, A.R., Rezaei, A.S., Askari, M., Shear Deformation Theories for Elastic Buckling of Fluid-infiltrated Porous Plates: An Analytical Approach, *Composite Structures* (2020), doi: https://doi.org/10.1016/j.compstruct.2020.112829

Shear Deformation Theories for Elastic Buckling of Fluid-infiltrated Porous Plates: An Analytical Approach

E. Sadeghi Rad[1], A. R. Saidi[2], A. S. Rezaei[3*], M. Askari[4]

[1]*Department of Mechanical Engineering, Yazd University, Yazd, Iran*
[2]*Department of Mechanical Engineering, Shahid Bahonar University of Kerman, Kerman, Iran*
[3]*Department of Mechanical and Aerospace Engineering, Sapienza University of Rome, 00184 Rome, Italy*
[4]*Department of Mechanical and Aerospace Engineering, Polytechnic University of Turin, 10129 Turin, Italy*

Abstract

In this paper, Reddy's higher-order and Mindlin's plate theories are used for buckling analysis of porous rectangular plates subjected to various mechanical loading with pores free/saturated by a fluid. Biot's theory of poroelasticity is employed to model the behaviour of fluid. Distribution of pores is assumed to vary through the thickness according to an asymmetric distribution. For each displacement field considered, five highly coupled partial differential equations are derived by means of variational principle. These systems of equations are first decoupled through an efficient method, and then solved analytically for Levy-type boundary conditions. Accuracy of the approach is examined by comparing the obtained results with those available in literature. Eventually, comprehensive parametric studies are provided to investigate the effects of geometrical parameters, boundary conditions, loading conditions, porosity coefficient and pore fluid compressibility on the buckling response of the system. The results suggest that a structure with higher equivalent rigidity is met, when its corresponding internal pores are saturated by fluid. The results of the current work can be considered as a benchmark for future studies.

Keywords: Buckling; fluid-infiltrated porous plate; Porosity; Higher-order theories; Analytical solutions.

1. Introduction

Extremely important industrial components are composed of plates due to their weight economy. For instance, plates' load/carrying capacity make then an appropriate candidate in aircraft industries. Besides, cellular materials have broad applications in diverse fields including acoustics, rock mechanics, and biophysics. The dynamic and static analyses of rather simple porous structures such as beams, plates and shells under various types of loading is of high research interest nowadays. Similarly, high stiffness to weight of porous materials is a significant element for manufacturing of products with weight constraints.

During the past two decades, a sizable number of papers have been dealing with the deflection, buckling and vibration analyses of structures composed of porous-cellular materials. Early studies [1–4] are conducted to realize the vibration characteristics of poroelastic systems when the fluid-loading is present; in this case, plates. These problems were particularly tackled from the viewpoint

* Corresponding author. Tel.: +39-3296918173
E-mail address: amirsajjad.rezaei@uniroma1.it (A. S. Rezaei)

of acoustics since benefits of such media is objectively shown in acoustics technologies. Some contributions [5–8] have been devoted to extract the resonant frequencies of linear porous-cellular thin-walled structures with different schemes for the porosity distribution. In this regard, researchers have followed various kinematic assumptions and solutions strategies in order to identify the motion patterns of the adopted system. To get a solid grasp of the problem from active control point of view, several researches [9–12] have been pursued. For instance, in Ref. [10] the nonlinear broadband vibration features of functionally graded piezoelectric smart plates are explored by simultaneous use of Galerkin and harmonic balance methods disclosing the existence of a threshold for having the nonlinear modal interactions.

Regarding the static analysis of porous structures, a fundamental investigation was carried by Biot [13], a pioneer of this field, to discuss the buckling behavior of fluid-saturated porous slabs under axial compression and by analogy, the application of the study for thermoelastic slabs is demonstrated as well. Deflection and buckling of plates of different geometries with continuous variation of porosity across the thickness have been subject to investigation [14,15] by considering nonlinear displacement function. Among the recent literature, a substantial number of articles [16–29] adopted shear deformation theories to obtain the static response of systems of interest. In particular, Tang et al. [22] showed higher critical buckling load is sustained by a two-directionally porous beam when pores distributed either near the mid-surface or two edges with respect to that of other distribution schemes, given identical porosity volume fractions. To appreciate the effect of nonlinearity on the buckling and post-buckling characteristics of porous plates, a few contributions [30,31] took Von Karman nonlinearity into account and the performance of the systems is evaluated with respect to the type of adopted porosity distribution with the help of post-buckling paths. In Refs. [32–34], authors have employed specific types of shear deformation theories such as refined higher-order and quasi-3D integral theories to carry out the thermal buckling analysis of porous thin-walled structures; providing insight into the effect of temperature field and porosity distribution on the critical buckling temperature. As an example, Zenkour and Aljadani [34] employed a refined higher-order theory along with Eringen's nonlocal elasticity theory to study the thermal buckling of actuated functionally graded piezoelectric porous nanoplates. Navier approach was utilized to analytically solve the governing equations, and thus extracting exact numerical results.

To the best of authors' knowledge, no work so far has investigated the effect of saturation condition on the buckling response of fluid-infiltrated porous rectangular plates via different plate theories. Kinematic assumptions made in the adopted theories, namely Mindlin and Reddy's third-order plate theory, give the possibility to extract the critical buckling load of plates under Levy-type boundary conditions with appropriate accuracy. Two conditions are assumed regarding the pores: fluid-saturated and free of fluid. Although several accurate numerical algorithms are available in the literature, the solution developed here guarantees the exactness of the results. To that end, the governing equations of the system are expressed in terms of some auxiliary functions offering the opportunity to obtain closed-form expressions of kinematic variables.

2. Problem modelling

2.1. Porous plate subjected to in-plane loading

Consider a rectangular plate, illustrated in Fig. 1(a), with area $a \times b$ and thickness h. The plate is made of porous materials, saturated by fluid, for which the material properties are considered to vary

along the thickness. To derive the mathematical relations, the origin of the coordinate system (x, y, z) is assumed at the middle surface of the plate. Fig. 1(b) shows the in-plane mechanical loads P_x (N/m) and P_y (N/m), which are applied to all edges of the plate.

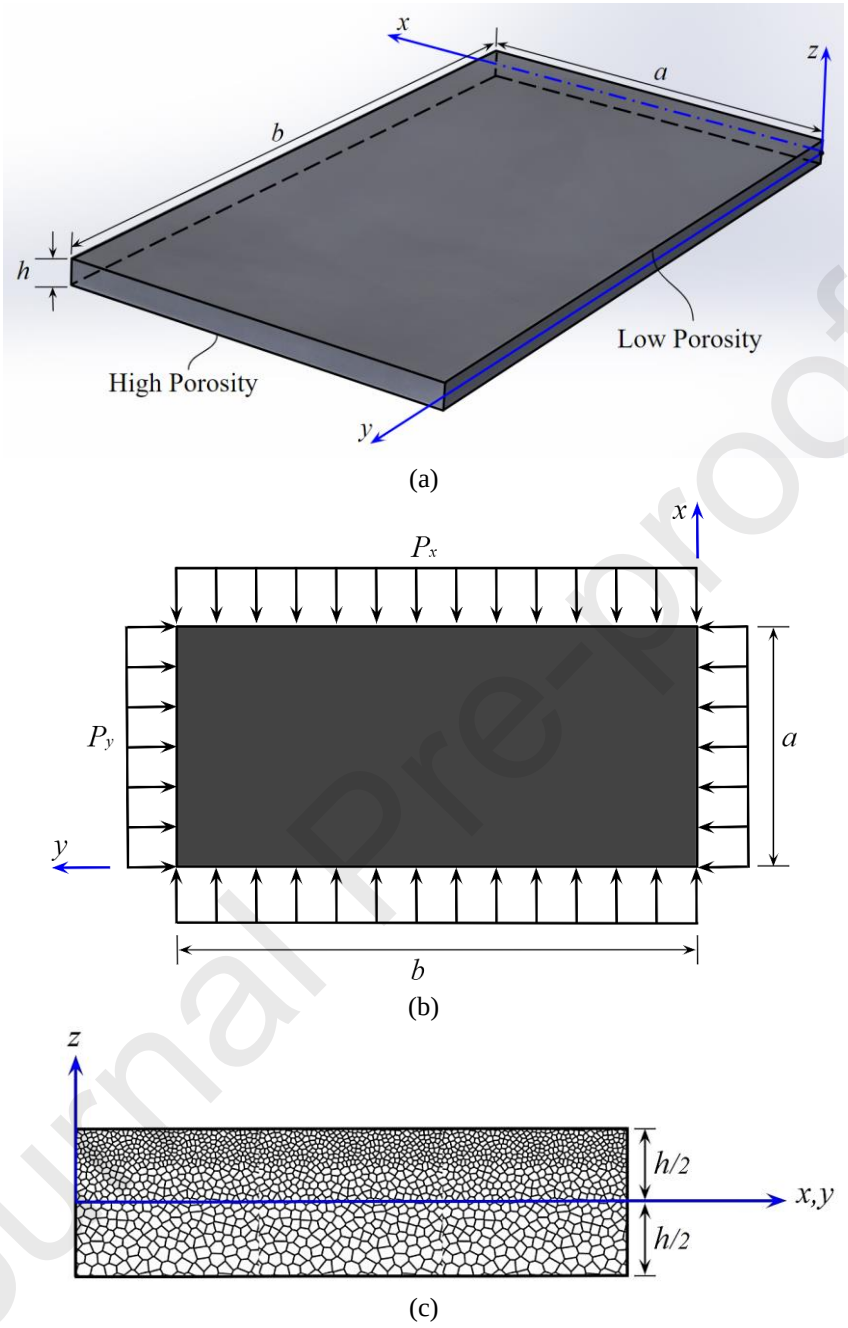

Fig. 1: (a) Sketch of the rectangular porous plate (b) In-plane loaded plate before buckling (top view) (c) Porosity distribution within plate cross-section

Different patterns have been considered in the literature to model the porosity distribution in porous materials and structure [5,6,9,14,21,35–37]. Here, it is assumed that the distribution of internal pores through the thickness of the plate is not uniform and follows an asymmetric rule with respect to mid-plane (see Fig. 1(c)). Thus, the material properties including Young's modulus $E(z)$ and shear elastic modulus $G(z)$ vary along the plate thickness as [5,37–39]:

$$G(z) = G_t\left(1 - e_1\cos\left(\frac{\pi z}{2h} + \frac{\pi}{4}\right)\right)$$
$$E(z) = E_t\left(1 - e_1\cos\left(\frac{\pi z}{2h} + \frac{\pi}{4}\right)\right) \quad (1)$$

in which the parameter e_1 is the porosity coefficient of the plate ($0 \le e_1 < 1$) and the change in the value of this parameter corresponds to the alteration of the size and density of internal pores, which causes variations in the mass density and elastic modulus of porous materials. The plate porosity coefficient is given as:

$$e_1 = 1 - \frac{G_b}{G_t} = 1 - \frac{E_b}{E_t} \quad (2)$$

Subscribes "*b*" and "*t*" are associated with the material properties at bottom ($z = -h/2$) and top ($z = +h/2$) faces of the plate, respectively. Assuming a constant value for the Poisson's ratio ν, the Young's modulus may be expressed as a function of shear modulus $E(z) = 2G(z)(1 + \nu)$. Equation (1) implies that the maximum and minimum values of $E(z)$ and $G(z)$ are occurred at the top and bottom faces of the porous plate, respectively. Note that setting the porosity coefficient to zero ($e_1 = 0$) is associated with no internal pores in the constituent material, while $e_1 = 1$ is physically meaningless.

2.2. Biot's poroelasticity theory

Internal pores in porous configurations are typically filled with a fluid such as gas or liquid. Due to the existence of this freely moving fluid throughout the porous structure, its mechanical response and properties could be modified and tailored in the desired manner [40]. Biot's constitutive equations comprehensively describe the behavior of porous media. These equations were obtained according to two main assumptions [40]:

I. An increase of pore pressure induces a dilation of pore.
II. Compression of the pore causes a rise of pore pressure.

According to the Biot's poroelasticity theory, the linear constitutive equations describing stress-strain relationships for a fluid-filled porous material can be expressed as [40]:

$$\sigma_{ij} = 2G(z)\varepsilon_{ij} + \frac{2G(z)\nu_u}{1 - 2\nu_u}\varepsilon\delta_{ij} - \alpha M\zeta\delta_{ij} \quad (3)$$

where σ_{ij} and ε_{ij} are the stress and strain components, respectively. The parameter M represents the Biot modulus, defined as the rise in the amount of fluid, ν_u is the undrained Poisson ratio, and ε denotes the volumetric strain. δ_{ij} is the Kronecker delta function, ζ is the variation of fluid volume content inside the pores, and α denotes the Biot coefficient of effective stress which is defined as $\alpha = \alpha(z) = 1 - G(z)/G_t$ and is obvious to be within the range of ($0 < \alpha < 1$) [41]. The parameters M and ν_u are defined in terms of other material properties as follows:

$$M = \frac{2G(z)(\nu_u - \nu)}{\alpha^2(1-2\nu_u)(1-2\nu)} \tag{4a}$$

$$\nu_u = \frac{3\nu + \alpha B(1-2\nu)}{3 - \alpha B(1-2\nu)} \tag{4b}$$

$$\alpha = 1 - \frac{G(z)}{G_t} = e_1 \cos\left(\frac{\pi z}{2h} + \frac{\pi}{4}\right) \tag{4c}$$

Here, B and ν represent the Skempton pore pressure coefficient and the drained Poisson's ratio ($\nu \leq \nu_u \leq 0.5$), respectively. It should be noted that the Skempton coefficient B is a measure, determining the degree of saturation in the porous body [42]. In particular, when the value of B equals zero, it refers to nearly absent pore fluid, thus estimating the porous solid as a dry porous medium.

In this study, the porous media is considered to operate under undrained condition, implying the entrapment of fluid in the porous solid accompanied by no variation in the fluid volume content in the internal pores, i.e. $\zeta = 0$. Therefore, the constitutive equations (3) for plane-stress condition take the form [40]:

$$\begin{Bmatrix} \sigma_{xx} \\ \sigma_{yy} \\ \sigma_{xy} \\ \sigma_{xz} \\ \sigma_{yz} \end{Bmatrix} = \begin{bmatrix} \hat{C}_{11} & \hat{C}_{12} & 0 & 0 & 0 \\ \hat{C}_{12} & \hat{C}_{11} & 0 & 0 & 0 \\ 0 & 0 & \hat{C}_{22} & 0 & 0 \\ 0 & 0 & 0 & \hat{C}_{22} & 0 \\ 0 & 0 & 0 & 0 & \hat{C}_{22} \end{bmatrix} \begin{Bmatrix} \varepsilon_{xx} \\ \varepsilon_{yy} \\ \varepsilon_{xy} \\ \varepsilon_{xz} \\ \varepsilon_{yz} \end{Bmatrix} \tag{5}$$

where $\hat{C}_{11}$, $\hat{C}_{12}$ and $\hat{C}_{22}$ are the material stiffness coefficients as:

$$\hat{C}_{11} = \frac{2G(z)}{1-\nu_u}, \qquad \hat{C}_{12} = \frac{2G(z)\nu_u}{1-\nu_u}, \qquad \hat{C}_{22} = KG(z) \tag{6}$$

in which ν_u is defined in Eq. (4b). Moreover, the parameter K indicates the shear correction factor that has to be considered in such analysis, to satisfy the free transverse shear stress conditions on the top and bottom surfaces of the plate. This matter is further discussed in the next section.

2.3. Displacement field

To consider the effects of transverse shear deformation on the system's response as well as making comparison studies, the first-order shear deformation theory (FSDT) and the third-order shear deformation theory (TSDT) are employed to derive the governing equations of motion. According to these theories, the mechanical displacement field at any point of the plate can be expressed as follows [43]:

$$\begin{Bmatrix} U_x(x,y,z) \\ U_y(x,y,z) \\ U_z(x,y,z) \end{Bmatrix} = \begin{Bmatrix} u_0(x,y) \\ v_0(x,y) \\ w_0(x,y) \end{Bmatrix} + z\begin{Bmatrix} \psi_x(x,y) \\ \psi_y(x,y) \\ 0 \end{Bmatrix} - \eta z^3 \begin{Bmatrix} \psi_x(x,y) + w_{0,x}(x,y) \\ \psi_y(x,y) + w_{0,y}(x,y) \\ 0 \end{Bmatrix} \tag{7}$$

in which u_x, u_y and u_z are the displacement components of any point of the plate along *x*, *y* and z axes, respectively. Also, u_0 and v_0 are in-plane displacements and w_0 is transverse displacement of the mid-plane of the plate, and ψ_x and ψ_y indicate the rotation functions with respect to *y* and *x* axes, respectively. Furthermore, α is a coefficient depending on the plate thickness and is equal to $\eta = 4/(3h^2)$ for TSDT. Setting $\eta = 0$ yields the displacement field of FSDT for which transverse shear deformation is assumed to be constant through the thickness direction, unlike TSDT. It should be noted that the value of the shear correction factor for FSDT is assumed to be $K = 5/6$, while TSDT does not require any shear correction factor, thereby setting $K = 1$ in Eq. (6) for this theory.

Using von Karman nonlinear hypothesis, the strain components associated with the displacement field (7) can be expressed as

$$\begin{Bmatrix}\varepsilon_{xx}\\ \varepsilon_{yy}\\ \gamma_{xy}\end{Bmatrix} = \begin{Bmatrix}\varepsilon^0_{xx}\\ \varepsilon^0_{yy}\\ \gamma^0_{xy}\end{Bmatrix} + z\begin{Bmatrix}\varepsilon^1_{xx}\\ \varepsilon^1_{yy}\\ \gamma^1_{xy}\end{Bmatrix} + z^3\begin{Bmatrix}\varepsilon^3_{xx}\\ \varepsilon^3_{yy}\\ \gamma^3_{xy}\end{Bmatrix};\quad \begin{Bmatrix}\gamma_{xz}\\ \gamma_{yz}\end{Bmatrix} = \begin{Bmatrix}\gamma^0_{xz}\\ \gamma^0_{yz}\end{Bmatrix} + z^2\begin{Bmatrix}\gamma^2_{xz}\\ \gamma^2_{yz}\end{Bmatrix} \tag{8}$$

in which

$$\begin{Bmatrix}\varepsilon^0_{xx}\\ \varepsilon^0_{yy}\\ \gamma^0_{xy}\\ \gamma^0_{xz}\\ \gamma^0_{yz}\end{Bmatrix} = \begin{Bmatrix} u_{0,x} + (w_{0,x})^2/2\\ v_{0,y} + (w_{0,y})^2/2\\ u_{0,y} + v_{0,x} + w_{0,x}w_{0,y}\\ \psi_x + w_{0,x}\\ \psi_y + w_{0,y}\end{Bmatrix};\quad \begin{Bmatrix}\varepsilon^1_{xx}\\ \varepsilon^1_{yy}\\ \gamma^1_{xy}\end{Bmatrix} = \begin{Bmatrix}\psi_{x,x}\\ \psi_{y,y}\\ \psi_{x,y} + \psi_{y,x}\end{Bmatrix} \tag{9a}$$

$$\begin{Bmatrix}\varepsilon^3_{xx}\\ \varepsilon^3_{yy}\\ \gamma^3_{xy}\end{Bmatrix} = -\eta\begin{Bmatrix}\psi_{x,x} + w_{0,xx}\\ \psi_{y,y} + w_{0,yy}\\ \psi_{x,y} + \psi_{y,x} + 2w_{0,xy}\end{Bmatrix};\quad \begin{Bmatrix}\gamma^2_{xz}\\ \gamma^2_{yz}\end{Bmatrix} = -3\eta\begin{Bmatrix}\psi_x + w_{0,x}\\ \psi_y + w_{0,y}\end{Bmatrix} \tag{9b}$$

It should be mentioned here that by setting $\eta = 0$ in Eq. (9b), and substituting the remaining non-zero expressions (i.e. the terms expressed in Eq. (9a)) in Equation (8), the strain components associated with FSDT will be obtained.

3. Governing stability equations

3.1. Variational principle

Here, the variational principle is applied to derive the differential equations governing equilibrium and buckling along with the natural boundary conditions of the plate subjected to in-plane loads. The principle for the present problem is of the form:

$$\delta(U + \Omega) = 0 \tag{10}$$

where δ is the variational operator, and U and Ω are the strain energy of the plate and the potential energy of external loads, respectively. In Eq. (10), the energy variations δU and $\delta\Omega$ can be obtained with the help of the definition of strain energy, the virtual work done by applied loads. Finally, by substituting the subsequent results of δU and $\delta\Omega$ in terms of the stress and strain components into the

variational principle, as well as performing some mathematical simplifications, the equilibrium equations can be obtained as follows:

$$\delta u_0: \quad N_{xx,x} + N_{xy,y} = 0 \tag{11a}$$

$$\delta v_0: \quad N_{xy,x} + N_{yy,y} = 0 \tag{11b}$$

$$\delta \phi_x: \quad M_{xx,x} + M_{xy,y} - Q_{xz} - \eta\left(\hat{P}_{xx,x} + \hat{P}_{xy,y}\right) + 3\eta\hat{R}_{xz} = 0 \tag{11c}$$

$$\delta \phi_y: \quad M_{xy,x} + M_{yy,y} - Q_{yz} - \eta\left(\hat{P}_{xy,x} + \hat{P}_{yy,y}\right) + 3\eta\hat{R}_{yz} = 0 \tag{11d}$$

$$\begin{aligned}\delta w_0: \quad & Q_{xz,x} + Q_{yz,y} + N_{xx}w_{0,xx} + 2N_{xy}w_{0,xy} + N_{yy}w_{0,yy} \\ & + \eta\left(\hat{P}_{xx,xx} + 2\hat{P}_{xy,xy} + \hat{P}_{yy,yy}\right) - 3\eta\left(\hat{R}_{xz,x} + \hat{R}_{yz,y}\right) = 0\end{aligned} \tag{11e}$$

where N_{ij}, M_{ij}, Q_{ij}, $\hat{P}_{ij}$ and $\hat{R}_{ij}$ are the resultant forces, moments, shear forces, higher-order moments and higher-order shear forces, in the given order; defined as follows:

$$(N_i, M_i) = \int_{-\frac{h}{2}}^{+\frac{h}{2}} \sigma_i(1, z)dz\,, \qquad i = \{xx, yy, xy\} \tag{12a}$$

$$Q_j = \int_{-\frac{h}{2}}^{+\frac{h}{2}} \sigma_j dz\,, \qquad j = \{xz, yz\} \tag{12b}$$

$$\hat{P}_i = \int_{-\frac{h}{2}}^{+\frac{h}{2}} \sigma_i z^3 dz\,, \qquad i = \{xx, yy, xy\} \tag{12c}$$

$$\hat{R}_j = \int_{-\frac{h}{2}}^{+\frac{h}{2}} \sigma_j z^2 dz\,, \qquad j = \{xz, yz\} \tag{12d}$$

Here, the higher order stress resultants (12c) and (12d) are seen in equilibrium equations (11) since these equations are derived based on TSDT; however, these higher-order terms would vanish for the case of FSDT (simply by setting $\eta = 0$ in Eqs. (11)).

Replacing the strain and stress fields given in Eqs. (5) and (8) into Equations. (12), the stress resultants can be rewritten as follows:

$$\begin{aligned}
N_{xx} &= a_{11}\varepsilon^0_{xx} + a_{12}\varepsilon^0_{yy} + b_{11}\varepsilon^1_{xx} + b_{12}\varepsilon^1_{yy} + d_{11}\varepsilon^3_{xx} + d_{12}\varepsilon^3_{yy} \\
N_{yy} &= a_{12}\varepsilon^0_{xx} + a_{11}\varepsilon^0_{yy} + b_{12}\varepsilon^1_{xx} + b_{11}\varepsilon^1_{yy} + d_{12}\varepsilon^3_{xx} + d_{11}\varepsilon^3_{yy} \\
N_{xy} &= a_{22}\gamma^0_{xy} + b_{22}\gamma^1_{xy} + d_{22}\gamma^3_{xy} \\
M_{xx} &= b_{11}\varepsilon^0_{xx} + b_{12}\varepsilon^0_{yy} + c_{11}\varepsilon^1_{xx} + c_{12}\varepsilon^1_{yy} - \eta f_{11}\varepsilon^3_{xx} - \eta f_{12}\varepsilon^3_{yy} \\
M_{yy} &= b_{12}\varepsilon^0_{xx} + b_{11}\varepsilon^0_{yy} + c_{12}\varepsilon^1_{xx} + c_{11}\varepsilon^1_{yy} - \eta f_{12}\varepsilon^3_{xx} - \eta f_{11}\varepsilon^3_{yy} \\
M_{xy} &= b_{22}\gamma^0_{xy} + c_{22}\gamma^1_{xy} - \eta f_{22}\gamma^3_{xy} \\
Q_{xz} &= a_{22}\gamma^0_{xz} + c_{22}\gamma^2_{xz} \\
Q_{yz} &= a_{22}\gamma^0_{yz} + c_{22}\gamma^2_{yz} \\
\hat{P}_{xx} &= d_{11}\varepsilon^0_{xx} + d_{12}\varepsilon^0_{yy} - \eta f_{11}\varepsilon^1_{xx} - \eta f_{12}\varepsilon^1_{yy} - \eta h_{11}\varepsilon^3_{xx} - \eta h_{12}\varepsilon^3_{yy} \\
\hat{P}_{yy} &= d_{12}\varepsilon^0_{xx} + d_{11}\varepsilon^0_{yy} - \eta f_{12}\varepsilon^1_{xx} - \eta f_{11}\varepsilon^1_{yy} - \eta h_{12}\varepsilon^3_{xx} - \eta h_{11}\varepsilon^3_{yy}
\end{aligned} \tag{13}$$

$$P_{xy} = d_{22}\gamma_{xy}^{0} - \eta f_{22}\gamma_{xy}^{1} - \eta h_{22}\gamma_{xy}^{3}$$
$$\hat{R}_{xz} = c_{22}\gamma_{xz}^{0} + f_{22}\gamma_{xz}^{2}$$
$$\hat{R}_{yz} = c_{22}\gamma_{yz}^{0} + f_{22}\gamma_{yz}^{2}$$

in which $A_{ij}, B_{ij}, C_{ij}, D_{ij}, F_{ij}, H_{ij}$ are the plate stiffness coefficients, defined as

$$\left(a_{ij}, b_{ij}, c_{ij}, d_{ij}, f_{ij}, h_{ij}\right) = \int_{-\frac{h}{2}}^{+\frac{h}{2}} (1, z, z^2, z^3, z^5, z^6)\, \hat{C}_{ij} dz, \qquad i,j = 1,2 \tag{14}$$

Considering Eq. (6) and (14), one easily learns:

$$\begin{pmatrix} a_{12} \\ b_{12} \\ c_{12} \\ d_{12} \\ f_{12} \\ h_{12} \end{pmatrix} = \begin{pmatrix} a_{11} \\ b_{11} \\ c_{11} \\ d_{11} \\ f_{11} \\ h_{11} \end{pmatrix} - 2 \begin{pmatrix} a_{22} \\ b_{22} \\ c_{22} \\ d_{22} \\ f_{22} \\ h_{22} \end{pmatrix} \tag{15}$$

3.2. Neighboring state approach

In buckling analysis, the plate is typically modeled as being perfectly flat before loading, i.e. no initial deflection over the entire surface of the plate. Increasing the in-plane loads, the transverse deflection as well as the in-plane deformations increase until suddenly the plate undergoes a deviation from the flat state to a state which is bowed in the z-direction. Calculation of the quasi-static load at which this change in behavior occurs (i.e. the buckling load) is the principle objective of this paper. In the following, the governing stability equations (GSE's) of rectangular plate are derived using the adjacent equilibrium criterion [44]. It is assumed that u_0^e, v_0^e, w_0^e, ψ_x^e and ψ_y^e are the displacement components of the equilibrium configuration of the plate and u_0^n, v_0^n, w_0^n, ψ_x^n and ψ_y^n are the virtual displacements of a neighboring state of the stable configuration. Thus, the entire displacements of a neighboring state may be found as

$$\begin{pmatrix} u_0 \\ v_0 \\ w_0 \\ \psi_x \\ \psi_y \end{pmatrix} \rightarrow \begin{pmatrix} u_0^e \\ v_0^e \\ w_0^e \\ \psi_x^e \\ \psi_y^e \end{pmatrix} + \begin{pmatrix} u_0^n \\ v_0^n \\ w_0^n \\ \psi_x^n \\ \psi_y^n \end{pmatrix} \tag{16}$$

Similar to Eqs. (16), the resultant moments and forces can be found to be the summation of those corresponded to the equilibrium and neighboring states as:

$$\begin{pmatrix} N_{xx} & M_{xx} & \hat{P}_{xx} \\ N_{xy} & M_{xy} & \hat{P}_{xy} \\ N_{yy} & M_{yy} & \hat{P}_{yy} \end{pmatrix} \equiv \begin{pmatrix} N_{xx}^e & M_{xx}^e & \hat{P}_{xx}^e \\ N_{xy}^e & M_{xy}^e & \hat{P}_{xy}^e \\ N_{yy}^e & M_{yy}^e & \hat{P}_{yy}^e \end{pmatrix} + \begin{pmatrix} N_{xx}^n & M_{xx}^n & \hat{P}_{xx}^n \\ N_{xy}^n & M_{xy}^n & \hat{P}_{xy}^n \\ N_{yy}^e & M_{yy}^n & \hat{P}_{yy}^n \end{pmatrix}$$
$$\begin{pmatrix} Q_{xz} & \hat{R}_{xz} \\ Q_{yz} & \hat{R}_{yz} \end{pmatrix} \equiv \begin{pmatrix} Q_{xz}^e & \hat{R}_{xz}^e \\ Q_{yz}^e & \hat{R}_{yz}^e \end{pmatrix} + \begin{pmatrix} Q_{xz}^n & \hat{R}_{xz}^n \\ Q_{yz}^n & \hat{R}_{yz}^n \end{pmatrix} \tag{17}$$

Substituting Eqs. (17) into Eqs. (11), omitting the terms with superscript *e* (since they satisfy the equilibrium condition), and similarly disregarding the non-linear terms with superscript *n* (because their effect is negligible with respect to the linear terms in the resulting equations) yield:

$$N^n_{xx,x} + N^n_{xy,y} = 0 \tag{18a}$$

$$N^n_{xy,x} + N^n_{yy,y} = 0 \tag{18b}$$

$$M^n_{xx,x} + M^n_{xy,y} - Q^n_{xz} - \eta\left(\hat{P}^n_{xx,x} + \hat{P}^n_{xy,y}\right) + 3\eta\hat{R}^n_{xz} = 0 \tag{18c}$$

$$M^n_{xy,x} + M^n_{yy,y} - Q^n_{yz} - \eta\left(\hat{P}^n_{xy,x} + \hat{P}^n_{yy,y}\right) + 3\eta\hat{R}^n_{yz} = 0 \tag{18d}$$

$$\begin{aligned} Q^n_{xz,x} + Q^n_{yz,y} + N^e_{xx}w^n_{0,xx} + 2N^e_{xy}w^n_{0,xy} + N^e_{yy}w^n_{0,yy} + \eta\left(\hat{P}^n_{xx,xx} + 2\hat{P}^n_{xy,xy} + \hat{P}^n_{yy,yy}\right) \\ - 3\eta\left(\hat{R}^n_{xz,x} + \hat{R}^n_{yz,y}\right) = 0 \end{aligned} \tag{18e}$$

Eqs. (18) represent five coupled partial differential equations governing the stability and buckling of the rectangular plate subjected to the in-plane loading, in which the parameters N^e_{xx}, N^e_{yy} and N^e_{xy} can be replaced by the pre-buckling forces acquired from equilibrium conditions (shown in Fig. 1(b)).

By replacing Eqs. (9) and (16) into the stress resultants (13), and the subsequent results into Eqs. (18), the GSE's will be obtained in terms of the neighboring displacement components as follows:

$$\begin{aligned} a_{11}u^n_{0,xx} + a_{12}v^n_{0,xy} + b_{11}\psi^n_{x,xx} + b_{12}\psi^n_{y,xy} + a_{22}\left(u^n_{0,y} + v^n_{0,x}\right)_{,y} + b_{22}\left(\psi^n_{x,y} + \psi^n_{y,x}\right)_{,y} \\ - \eta d_{22}\left(\psi^n_{x,y} + \psi^n_{y,x} + 2w^n_{0,xy}\right)_{,y} - \eta d_{11}\left(\psi^n_{x,x} + w^n_{0,xx}\right)_{,x} \\ - \eta d_{12}\left(\psi^n_{y,y} + w^n_{0,yy}\right)_{,x} = 0 \end{aligned} \tag{19a}$$

$$\begin{aligned} a_{11}v^n_{0,yy} + a_{12}u^n_{0,xy} + b_{11}\psi^n_{y,yy} + b_{12}\psi^n_{x,xy} + a_{22}\left(u^n_{0,y} + v^n_{0,x}\right)_{,x} + b_{22}\left(\psi^n_{x,y} + \psi^n_{y,x}\right)_{,x} \\ - \eta d_{22}\left(\psi^n_{x,y} + \psi^n_{y,x} + 2w^n_{0,xy}\right)_{,x} - \eta d_{11}\left(\psi^n_{y,y} + w^n_{0,yy}\right)_{,y} \\ - \eta d_{12}\left(\psi^n_{x,x} + w^n_{0,xx}\right)_{,y} = 0 \end{aligned} \tag{19b}$$

$$\begin{aligned} [b_{11} - \eta d_{11}]u^n_{0,xx} + [b_{12} - \eta d_{12}]v^n_{0,xy} + [c_{11} - \eta f_{11}]\psi^n_{x,xx} + [c_{12} - \eta f_{12}]\psi^n_{y,xy} \\ + [b_{22} - \eta d_{22}]\left(u^n_{0,y} + v^n_{0,x}\right)_{,y} + [c_{22} - \eta f_{22}]\left(\psi^n_{x,y} + \psi^n_{y,x}\right)_{,y} \\ - \eta[f_{22} - \eta h_{22}]\left(\psi^n_{x,y} + \psi^n_{y,x} + 2w^n_{0,xy}\right)_{,y} \\ - \eta[f_{11} - \eta h_{11}]\left(\psi^n_{x,x} + w^n_{0,xx}\right)_{,x} - \eta[f_{12} - \eta h_{12}]\left(\psi^n_{y,y} + w^n_{0,yy}\right)_{,x} \\ - [a_{22} - 6\eta c_{22} + 9\eta^2 f_{22}]\left(\psi^n_x + w^n_{0,x}\right) = 0 \end{aligned} \tag{19c}$$

$$\begin{aligned} [b_{11} - \eta d_{11}]v^n_{0,yy} + [b_{12} - \eta d_{12}]u^n_{0,xy} + [c_{11} - \eta f_{11}]\psi^n_{y,yy} + [c_{12} - \eta f_{12}]\psi^n_{x,xy} \\ + [b_{22} - \eta d_{22}]\left(u^n_{0,y} + v^n_{0,x}\right)_{,x} + [c_{22} - \eta f_{22}]\left(\psi^n_{x,y} + \psi^n_{y,x}\right)_{,x} \\ - \eta[f_{22} - \eta h_{22}]\left(\psi^n_{x,y} + \psi^n_{y,x} + 2w^n_{0,xy}\right)_{,x} \\ - \eta[f_{11} - \eta h_{11}]\left(\psi^n_{y,y} + w^n_{0,yy}\right)_{,y} - \eta[f_{12} - \eta h_{12}]\left(\psi^n_{x,x} + w^n_{0,xx}\right)_{,y} \\ - [a_{22} - 6\eta c_{22} + 9\eta^2 f_{22}]\left(\psi^n_y + w^n_{0,y}\right) = 0 \end{aligned} \tag{19d}$$

$$\begin{aligned}\eta\Big\{&d_{11}\left(u^n_{0,xxx}+v^n_{0,yyy}\right)+d_{12}\left(u^n_{0,xyy}+v^n_{0,yxx}\right)+f_{11}\left(\psi^n_{x,xxx}+\psi^n_{y,yyy}\right)\\&+f_{12}\left(\psi^n_{x,xyy}+\psi^n_{y,yxx}\right)-\eta h_{11}\left[\left(\psi^n_{x,x}+w^n_{0,xx}\right)_{,xx}+\left(\psi^n_{y,y}+w^n_{0,yy}\right)_{,yy}\right]\\&-\eta h_{12}\left[\left(\psi^n_{y,y}+w^n_{0,yy}\right)_{,xx}+\left(\psi^n_{x,x}+w^n_{0,xx}\right)_{,yy}\right]+2d_{22}\left(u^n_{0,y}+v^n_{0,x}\right)_{,xy}\\&+2f_{22}\left(\psi^n_{x,y}+\psi^n_{y,x}\right)_{,xy}-2\eta h_{22}\left(\psi^n_{x,y}+\psi^n_{y,x}+2w^n_{0,xy}\right)_{,xy}\Big\}\\&+\left(a_{22}-6\eta c_{22}+9\eta^2 f_{22}\right)\left[\left(\psi^n_x+w^n_{0,x}\right)_{,x}+\left(\psi^n_y+w^n_{0,y}\right)_{,y}\right]+N^e_{xx}w^n_{0,xx}\\&+2N^e_{xy}w^n_{0,xy}+N^e_{yy}w^n_{0,yy}=0\end{aligned}\tag{19e}$$

Here, GSE's of rectangular plates subjected to in-plane compressive loads acting on the mid-plane edges have been extracted, which are highly coupled.

Furthermore, the mechanical boundary conditions of the plate's edges can be obtained from the adjacent equilibrium criterion, as given in Table 1.

Table 1: Essential and natural boundary conditions correspond to FSDT and TSDT

Edge Condition	Expressions
TSDT	
Simply Supported (S)	$N^n_{xx}=v^n_0=w^n_0=\psi^n_x=M^n_{yy}=P^n_{yy}=0$
Clamped (C)	$u^n_0=v^n_0=w^n_0=w^n_{0,y}=\psi^n_x=\psi^n_y=0$
Free (F)	$N^n_{yy}=N^n_{xy}=M^n_{yy}=P^n_{yy}=M^n_{xy}-\eta P^n_{xy}$ $=\left(Q^n_{yz}-3\eta R^n_{yz}\right)+\eta\left(2P^n_{xy,x}+P^n_{yy,y}\right)+N^e_{yy}w^n_{0,y}=0$
FSDT	
Simply Supported (S)	$N^n_{xx}=v^n_0=w^n_0=\psi^n_x=M^n_{yy}=0$
Clamped (C)	$u^n_0=v^n_0=w^n_0=\psi^n_x=\psi^n_y=0$
Free (F)	$N^n_{yy}=N^n_{xy}=M^n_{yy}=M^n_{xy}=Q^n_{yz}+N^e_{yy}w^n_{0,y}=0$

4. Solution procedure

4.1. Decoupling strategy

To analytically investigate the buckling problem of the plate with different boundary conditions, the GSE's (19) are first decoupled by employing a simple and efficient technique. As the first step of the decoupling procedure, the four new auxiliary functions ϕ_1, ϕ_2, ϕ_3 and ϕ_4 are defined as follows:

$$\begin{pmatrix}\phi_1\\ \phi_2\\ \phi_3\\ \phi_4\end{pmatrix}=\begin{pmatrix}u^n_{0,x}+v^n_{0,y}\\ u^n_{0,y}-v^n_{0,x}\\ \psi^n_{x,x}+\psi^n_{y,y}\\ \psi^n_{x,y}-\psi^n_{y,x}\end{pmatrix}\tag{20}$$

Considering Eq. (15), and the substitution of the auxiliary functions into the GSE's (19), one obtains:

$$a_{11}\phi_{1,x}+a_{22}\phi_{2,y}+\tilde{b}_{11}\phi_{3,x}+\tilde{b}_{22}\phi_{4,y}-\eta d_{11}\nabla^2\left(w^n_{0,x}\right)=0\tag{21a}$$

$$a_{11}\phi_{1,y} + a_{22}\phi_{2,x} + \tilde{b}_{11}\phi_{3,y} + \tilde{b}_{22}\phi_{4,x} - \eta d_{11}\nabla^2\left(w_{0,y}^n\right) = 0 \tag{21b}$$

$$\tilde{b}_{11}\phi_{1,x} + \tilde{b}_{22}\phi_{2,y} + \tilde{c}_{11}\phi_{3,x} + \tilde{c}_{22}\phi_{4,y} - \tilde{a}_{22}\left[\psi_x^n + w_{0,x}^n\right] - \tilde{h}_{11}\nabla^2\left(w_{0,x}^n\right) = 0 \tag{21c}$$

$$\tilde{b}_{11}\phi_{1,y} - \tilde{b}_{22}\phi_{2,x} + \tilde{c}_{11}\phi_{3,y} - \tilde{c}_{22}\phi_{4,x} - \tilde{a}_{22}\left[\psi_y^n + w_{0,y}^n\right] - \tilde{h}_{11}\nabla^2\left(w_{0,y}^n\right) = 0 \tag{21d}$$

$$\begin{aligned}\eta d_{11}\nabla^2(\phi_1) + \tilde{h}_{11}\nabla^2(\phi_3) - \eta^2 h_{11}\nabla^4(w_0^n) + \tilde{a}_{22}[\nabla^2(w_0^n) + \phi_3] + N_{xx}^e w_{0,xx}^n \\ + 2N_{xy}^e w_{0,xy}^n + N_{yy}^e w_{0,yy}^n = 0\end{aligned} \tag{21e}$$

In Eqs. (21), ∇^2 is the two-dimensional Laplace operator in the Cartesian reference system, and the coefficients $\tilde{a}_{22}$, $\tilde{b}_{11}$, $\tilde{b}_{22}$, $\tilde{c}_{11}$, $\tilde{c}_{22}$ and $\tilde{h}_{11}$ are given in the relation (A.1) of Appendix A.

Considering $\tilde{b}_{22} = \tilde{b}_{11}a_{22}/a_{11}$, Eqs. (21a) and (21b) can be rewritten as:

$$\tilde{b}_{11}\phi_{1,x} + \tilde{b}_{22}\phi_{2,y} = -\left(\frac{(\tilde{b}_{11})^2}{a_{11}}\right)\phi_{3,x} - \left(\frac{\tilde{b}_{11}\tilde{b}_{22}}{a_{11}}\right)\phi_{4,y} + \left(\frac{\eta d_{11}\tilde{b}_{11}}{a_{11}}\right)\nabla^2 w_{0,x}^n \tag{22a}$$

$$\tilde{b}_{11}\phi_{1,y} + \tilde{b}_{22}\phi_{2,x} = -\left(\frac{(\tilde{b}_{11})^2}{a_{11}}\right)\phi_{3,y} - \left(\frac{\tilde{b}_{11}\tilde{b}_{22}}{a_{11}}\right)\phi_{4,x} + \left(\frac{\eta d_{11}\tilde{b}_{11}}{a_{11}}\right)\nabla^2 w_{0,y}^n \tag{22b}$$

Deriving Eqs. (22a) and (22b) with respect to in-plane coordinates, and carrying out some algebraic operations gives:

$$\nabla^2\phi_1 = -\frac{\tilde{b}_{11}}{a_{11}}\nabla^2\phi_3 + \frac{\eta d_{11}}{a_{11}}\nabla^4 w_0^n \tag{23a}$$

$$\nabla^2\phi_2 = \frac{\tilde{b}_{11}}{a_{11}}\nabla^2\phi_4 \tag{23b}$$

On the other hand, by using Eqs. (22) and (23), the last three equations of the system of Eqs. (21) can be rewritten as:

$$\hat{c}_{11}\phi_{3,x} + \hat{b}_{11}\phi_{4,y} - \hat{a}_{11}(\psi_x^n + w_{0,x}^n) - \hat{h}_{11}\nabla^2 w_{0,x}^n = 0 \tag{24a}$$

$$\hat{c}_{11}\phi_{3,y} - \hat{b}_{11}\phi_{4,x} - \hat{a}_{11}(\psi_y^n + w_{0,y}^n) - \hat{h}_{11}\nabla^2 w_{0,y}^n = 0 \tag{24b}$$

$$\hat{h}_{11}\nabla^2\phi_3 - \hat{f}_{11}\nabla^4 w_0^n + \hat{a}_{11}(\nabla^2 w_0^n + \phi_3) + N_{xx}^e w_{0,xx}^n + 2N_{xy}^e w_{0,xy}^n + N_{yy}^e w_{0,yy}^n = 0 \tag{24c}$$

in which the coefficients $\hat{a}_{11}$, $\hat{b}_{11}$, $\hat{c}_{11}$, $\hat{f}_{11}$ and $\hat{h}_{11}$ are given in relations (A.2) of Appendix A.

It is clear that Equations (24) have been obtained only in terms of the rotation functions ψ_x^n and ψ_y^n as well as the transverse displacement w_0^n, and these equations are independent of the in-plane displacements. By applying some mathematical operations to these three coupled equations (24), they are converted to the following two independent differential equations:

$$\hat{b}_{11}\nabla^2\phi_4 - \hat{a}_{11}\phi_4 = 0 \tag{25a}$$

$$\begin{aligned}\bar{c}_{11}\nabla^6 w_0^n - \bar{d}_{11}\nabla^4 w_0^n = (\hat{c}_{11}/\hat{a}_{11})\nabla^2\left(N_{xx}^0 w_{0,xx}^n + 2N_{xy}^0 w_{0,xy}^n + N_{yy}^0 w_{0,yy}^n\right) \\ - \left(N_{xx}^0 w_{0,xx}^n + 2N_{xy}^0 w_{0,xy}^n + N_{yy}^0 w_{0,yy}^n\right)\end{aligned} \tag{25b}$$

where the coefficients $\bar{c}_{11}$ and $\bar{d}_{11}$ are expressed in Eqs. (A.3) of Appendix A.

The terms N_{xx}^{0}, N_{xy}^{0} and N_{yy}^{0} in Equation (25b) are the pre-buckling in-plane loads which can be determined using the equilibrium condition. In the current study, it is assumed that the plate is subjected to in-plane loading in two directions, as shown in Fig. 1(b), thus:

$$\begin{pmatrix} N_{xx}^{0} \\ N_{yy}^{0} \\ N_{xy}^{0} \end{pmatrix} = -\begin{pmatrix} P_x \\ P_y \\ 0 \end{pmatrix} \tag{26}$$

where P_x and P_y are the in-plane forces (N/m) acting on the edges of the mid-plane. Substituting Eq. (26) into Eqs. (25) results in

$$\hat{b}_{11}\nabla^2\phi_4 - \hat{a}_{11}\phi_4 = 0 \tag{27a}$$

$$\bar{c}_{11}\nabla^6 w_0^n - \bar{d}_{11}\nabla^4 w_0^n = -(\hat{c}_{11}/\hat{a}_{11})\nabla^2\left(P_x w_{0,xx}^n + P_y w_{0,yy}^n\right) - \left(P_x w_{0,xx}^n + P_y w_{0,yy}^n\right) \tag{27b}$$

As is obvious, there are two independent load parameters in Equation (27b). By assuming $P_y = RP_x$ in which R is a non-dimensional parameter, it simplifies as:

$$\bar{c}_{11}\nabla^6 w_0^n - \bar{d}_{11}\nabla^4 w_0^n = -(\hat{c}_{11}/\hat{a}_{11})\nabla^2\left(P_x w_{0,xx}^n + RP_x w_{0,yy}^n\right) - \left(P_x w_{0,xx}^n + RP_x w_{0,yy}^n\right) \tag{28}$$

The parameter R signify the loading conditions. In particular, when R is positive, the plate is under biaxial compression and negative values imply tensile loading in the y direction whereas the plate is under compression along the x direction. Clearly, setting $R = 0$ means that the plate is under uniaxial compressive loading along the x direction. These three different loading conditions are shown in Fig. 2.

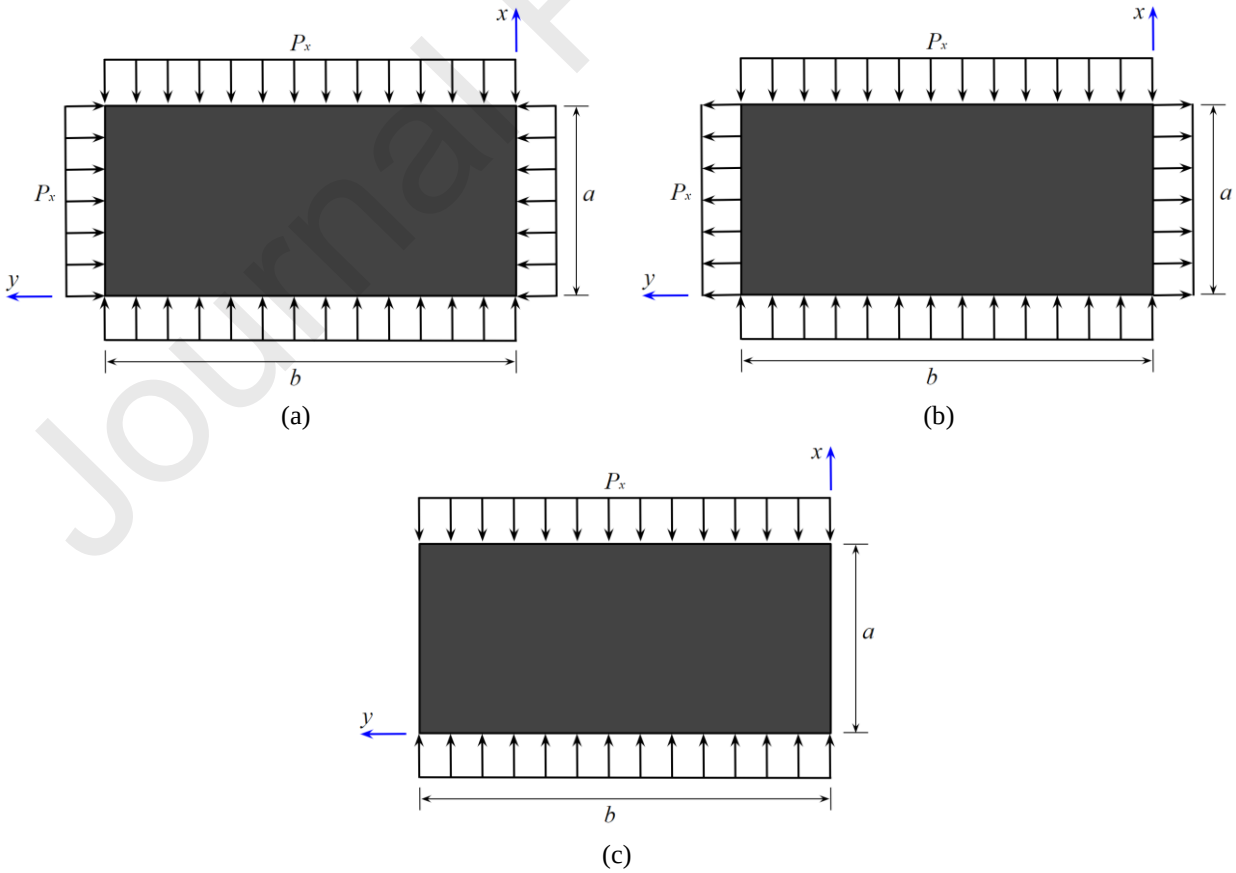

Fig. 2: Rectangular plate under mechanical in-plane loading on its edges a) $R = 1$, b) $R = -1$, and c) $R = 0$

4.2. Levy-type solution

Consider a rectangular plate with simply supported edges at $x = 0$ and $x = a$, whilst the other two edges can adopt any arbitrary classical condition. Based on this assumption, six possible boundary conditions, namely S-F-S-F, S-S-S-S, S-C-S-C, S-S-S-C, S-C-S-F and S-S-S-F may be imagined, as shown in Fig. 3. The letters (S), (C) and (F) refer to simply-supported, clamped free Boundary conditions, respectively.

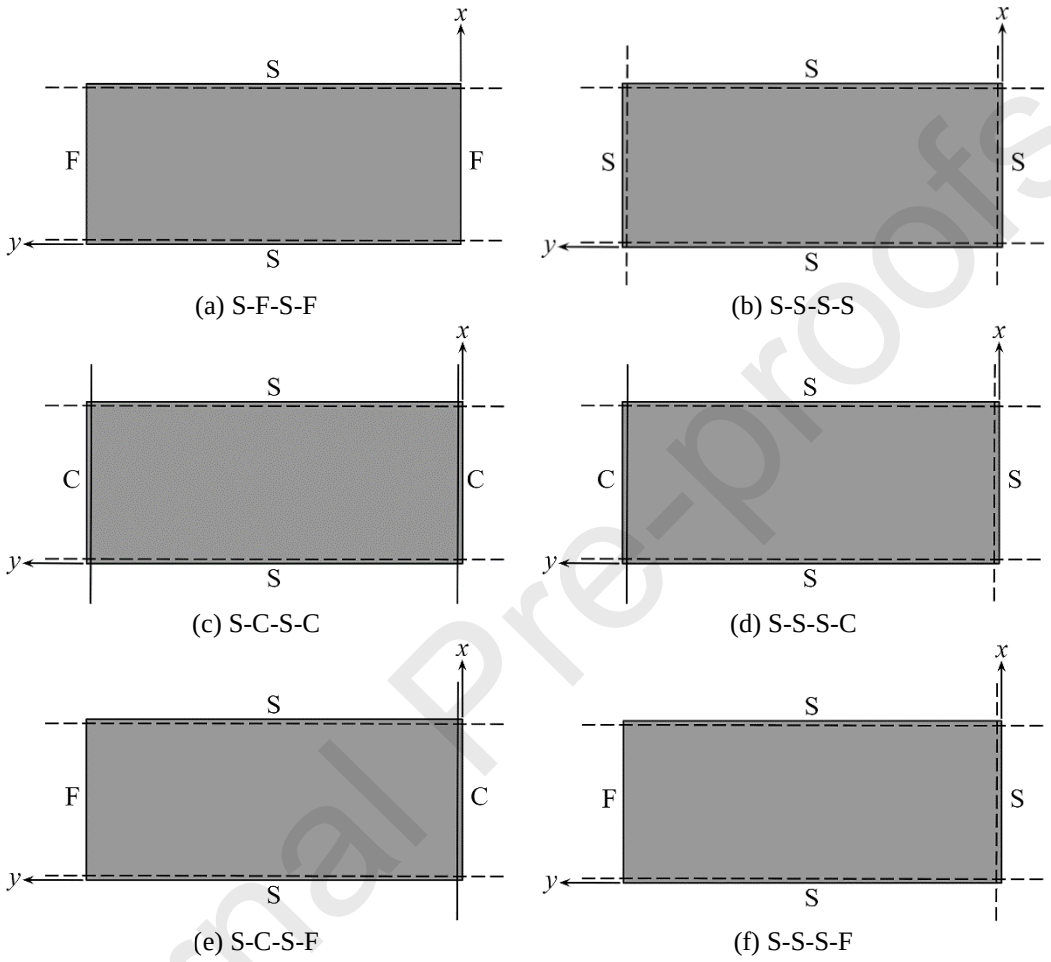

(a) S-F-S-F (b) S-S-S-S

(c) S-C-S-C (d) S-S-S-C

(e) S-C-S-F (f) S-S-S-F

Fig. 3: Various Levy-type boundary conditions

According to the Levy approach, the following expansions for the transverse displacement and the auxiliary function ϕ_4 suffice to satisfy the simply-supported boundary conditions at the edges $x = 0$ and $x = a$, as:

$$w_0^n(x,y) = \sum_{m=1}^{\infty} F_m(y) \sin\left(\frac{m\pi x}{a}\right) \tag{29a}$$

$$\phi_4(x,y) = \sum_{m=1}^{\infty} S_m(y) \cos\left(\frac{m\pi x}{a}\right) \tag{29b}$$

where the function $F_m(y)$ is the buckling shape function in the y direction. Also, the parameter m indicates the number of half-waves along the x direction of buckling mode shape.

Substituting the proposed series solutions (29) into Eqs. (28a) and (29) results in:

$$\zeta_1 \frac{d^6}{dy^6} F_m(y) + \zeta_2 \frac{d^4}{dy^4} F_m(y) + \zeta_3 \frac{d^2}{dy^2} F_m(y) + \zeta_4 F_m(y) = 0 \tag{30a}$$

$$\zeta_5 \frac{d^2}{dy^2} S_m(y) + \zeta_6 S_m(y) = 0 \tag{30b}$$

The parameters ζ_i (i =1, 2, 3, 4, 5, 6) are defined in Eq. (A.4) of Appendix A. As seen, two homogenous ordinary differential equations with constants coefficients are obtained. The corresponding solutions for these equations are:

$$F_m(y) = T_1 \cosh(\lambda_1 y) + T_2 \sinh(\lambda_1 y) + T_3 \cosh(\lambda_2 y) + T_4 \sinh(\lambda_2 y) + T_5 \cosh(\lambda_3 y) + T_6 \sinh(\lambda_3 y) \tag{30a}$$

$$S_m(y) = T_7 \cosh(\lambda_4 y) + T_8 \sinh(\lambda_4 y) \tag{30b}$$

Here, the parameters T_i (i = 1, 2, 3, 4, 5, 6, 7, 8) are unknown coefficients, $\lambda_4 = \sqrt{(m\pi/a)^2 + \hat{a}_{11}/\hat{b}_{11}}$, and $\lambda_j = \pm\sqrt{\Xi_j}$ (j =1, 2, 3) with the parameters Ξ_j (j =1, 2, 3) being the roots of the following characteristic equation associated with Equation (30a):

$$\zeta_1 t^3 + \zeta_2 t^2 + \zeta_3 t + \zeta_4 = 0 \tag{32}$$

Applying various boundary conditions, given in Table 1, eight homogenous algebraic equations are obtained in terms of the critical buckling load P_x as well as the unknown coefficients T_i. For a nontrivial solution of the system, the determinant of the eight-order coefficient matrix vanishes, which yields a characteristic equation in terms of P_x. Solving the resulting equation, the critical buckling load $P_{\mathrm{cr}}(m)$, associated with the mth buckling mode, will be calculated.

5. Results and discussion

5.1. Validation

For the sake of verification of the presented formulation, two examples are provided here. Table 2 compares the extracted results for both FSDT and TSDT with the spline strip solution of Shufrin and Eisenberger [45] for the buckling response of a simply supported isotropic rectangular plate. The results are given for three different thickness-length ratios, namely 0.1, 0.2 and 0.3. Although the discrepancies between the corresponding FSDT results for rather thin plates ($h/b = 0.1$) and those reported in Ref. [45] are negligible, one observes that the differences grow by the increase in value of thickness-length ratio. This is due to the fact that FSDT is suitable for moderately thick plates for which the effect of shear forces is not influential. In fact, for thicker plates, more significant discrepancies are yielded due to lack of precise value for shear correction factor. However, the differences do not exceed 2%. The discrepancies of TSDT model with respect to the cited article are incredibly small, implying the efficiency of the theory for modelling rather thick structures. Therefore, both theories are capable of providing accurate data, if utilized in the proper thickness range.

Table 2: Verification of buckling load parameter, $P_{cr} = \frac{\cdot_{cr}\cdot}{\pi^2 D}$, for S-S-S-S plate with those of Ref. [45]

Aspect ratio (a/b)	Thickness-length ratio (h/b)	Source	Loading Type		
			(-1, 0), P_x	(0, -1), P_y	(-1, -1), P_x, P_y
1	0.1	FSDT [45]	3.7865	3.7865	1.8932
		FSDT (Present)	3.7842	3.7842	1.8971
		TSDT [45]	3.7866	3.7866	1.8933
		TSDT (Present)	3.7854	3.7854	1.8920
	0.2	FSDT [45]	3.2637	3.2637	1.6327
		FSDT (Present)	3.2870	3.2870	1.6435
		TSDT [45]	3.2653	3.2653	1.6327
		TSDT (Present)	3.2652	3.2652	1.6325
	0.3	FSDT [45]	2.6586	2.6586	1.3293
		FSDT (Present)	2.6881	2.6881	1.3440
		TSDT [45]	2.6586	2.6586	1.3293
		TSDT (Present)	2.6586	2.6586	1.3292
2	0.1	FSDT [45]	3.7865	1.5093	1.2074
		FSDT (Present)	3.7942	1.5113	1.2090
		TSDT [45]	3.7866	1.5093	1.2075
		TSDT (Present)	3.7862	1.5075	1.2074
	0.2	FSDT [45]	3.2637	1.3694	1.0955
		FSDT (Present)	3.2870	1.3759	1.1008
		TSDT [45]	3.2653	1.3697	1.0958
		TSDT (Present)	3.2653	1.3696	1.0956
	0.3	FSDT [45]	2.5726	1.1862	0.9498
		FSDT (Present)	2.6181	1.1973	0.9578
		TSDT [45]	2.5839	1.1873	0.9498
		TSDT (Present)	2.5839	1.1872	0.9498

The results associated with other boundary conditions are validated by a comparison study provided in Table 3. All six possible Levy-type boundary conditions are considered for a homogenous plate of the aspect ratio $a/b = 0.5$ and the thickness-length ratio $h/b = 0.1$. As seen, the results of the FSDT theory are closer to those from the analytical solution of Ref. [46] due to the similarity between the adopted theory. Full agreement between the FSDT results for a plate under S-S-S-S and S-C-S-C boundary conditions subjected to both uniaxial and biaxial compressive loading and those of Ref. [46] is observed, and the difference for other boundary conditions, though negligible, could be attributed to the different choice of shear correction factor in the corresponding studies. Thus, the reliability of the presented analytical solution is approved and highlighted.

Having completed the verification examples, parametric studies covering the effects of various parameters on the buckling response of porous plates are carried out in the following section.

Table 3: Verification of buckling load parameter, $\bar{P}_{cr} = \frac{P_{cr}a^2}{D}$, with those of Ref. [46] ($a/b = 0.5$, $h/b = 0.1$)

Loading Type	Boundary Conditions	Source		
		FSDT [46]	FSDT (Present)	TSDT (Present)
$R = 0$	S-F-S-F	9.325573	9.323059	9.310392
	S-S-S-S	14.915722	14.915722	14.895564
	S-C-S-C	18.055467	18.055467	18.019092
	S-S-S-C	16.247894	16.243511	16.216309
	S-C-S-F	10.642566	10.633351	10.619809
	S-S-S-F	10.408425	10.395851	10.387661
$R = 1$	S-F-S-F	9.060047	9.050059	9.037392
	S-S-S-S	11.932578	11.932578	11.909626
	S-C-S-C	13.969074	13.969074	13.937742
	S-S-S-C	12.745925	12.735461	12.721909
	S-C-S-F	9.452941	9.445801	9.445909
	S-S-S-F	9.384918	9.369371	9.369371

5.2. Parametric studies

Here, a number of parametric studies have been provided to realize the influence of different parameters on the buckling load of the rectangular porous plate under studying. To extract numerical results, the system is assumed to be made of *Tennessee marble* with the following properties [40]:

$$G = 24 \text{ GPa} \;\&\; \upsilon = 0.25 \;\&\; B = 0.51$$

In Tables 4-9, the buckling load is calculated for rectangular porous plates of different aspect ratio and thickness-length ratio for several porosity coefficients under various saturation and loading conditions. Each table is devoted to presenting the data for one of the six possible Levy-type boundary conditions. Note that only the principal buckling mode is given in the tables. Several point could be realized from the tables including the effect of geometrical parameters, loading and saturation on the critical buckling load of the plate.

Primarily, three different loading conditions are brought in the tables: i) $R = -1$ describing uniform tensile loading acting on vertical edges with the same magnitude of that acting on the horizontal edges, ii) $R = 0$ implying the absence of loading on vertical edges, and iii) $R = 1$ describing compressive loading of the same magnitude on all edges. As expected, the third type of loading drives the system towards buckling failure earlier with respect to other two cases, followed by the second and the first type, in the order given. In fact, exceeding from the safety threshold in terms of stress, when tensile loading act on vertical edges occur the latest due to the induction of higher equivalent rigidity. Obviously, the magnitude of force required for reaching the unstable phase, i.e. the buckling load is related to the type of constraints applied on edges. For instance, if an edge is clamped, higher loads are requited for buckling as compared to the similar system with this edge adopting free and simply support boundary conditions. This indeed is concerned with degrees of freedom being divested by the boundary condition of the edge.

Some of the buckling loads P_{cr} shown in the tables are accompanied by the * symbol, implying the occurrence of buckling in a higher mode, meaning that the first mode extracted from the mathematical

framework presented above is not essentially the fundamental buckling mode, and the phenomenon may take place by exerting even a smaller P_{cr}, in terms of magnitude, which is produced by higher modes. In a general sense, the buckling mode transition is seen for the plates with stiffer edge conditions including S-C-S-C, S-S-S-C and S-S-S-S, especially when the plates undergo dissimilar loading types on it corresponding horizonal and vertical edges. For instance, a S-C-S-C plate under first and second type of loading (see the previous paragraph), where P_y is either tensile or absent, first mode is no longer the principal mode.

The results brought in the tables are extracted from two different theories, which are utilized in this study. All the data provided are extracted by both first-order and third-order shear deformation theories. Discrepancies between the results of these two theories becomes more evident as the thickness-length ratio increases, as anticipated. In fact, the effect of transverse shear deformations is bolder in thicker structures, and consequently higher-order models are required to accurately model them. Besides, the difference between the results of two theories are comparatively more considerable for more constrained plates though the discrepancies are still incredibly small even for a fully constrained configuration, i.e. S-C-S-C boundary condition.

The effect of geometrical parameters on the critical buckling load of the plates under studying is also demonstrated in tables. Tables imply that an increase in the value of thickness-length ratio h/a, when all other parameters are fixed, leads to higher buckling loads. The underlying reason may be understood intuitively since higher h/a is in direct correspondence to the equivalent rigidity of the plate. Based on the tables, doubling the value of h/a is accompanied by a few hundred percent increase in P_{cr}. Thus, higher thicknesses may be considered as a qualified solution for avoiding low P_{cr} in systems; however, the geometrical and weight constraints of the desired component are of importance as well. Regarding the effect of aspect ratio on the output, one observes that P_{cr} rises as a/b increases for all boundary conditions expect for the plate with vertical edges free. In fact, the plate under S-F-S-F boundary condition behaves like a beam which becomes slenderer by increase in a/b, and thereby a decrease in P_{cr}. Sensitivity of buckling mode to the aspect ratio is exhibited in Fig. 4, where the variation of buckling load against a/b for different porosity coefficients and numbers of half-waves m is plotted. As illustrated, buckling may occur at higher modes as aspect ratio rises. This trend is shown to remain true regardless of the porosity coefficient e_1.

The main contribution of this work is related to the effect of the porosity and saturation condition on the critical buckling load of rectangular plates. These effects can be realised from the data given the tables. As earlier stated, higher porosity coefficient e_1 is linked to higher density of pores across the plate's thickness. In fact, when e_1 rises, the skeleton material occupies a smaller volume, and thereby smaller effective stiffness. This justifies the trend observed in the tables being the decrease in P_{cr} with an increase in the porosity coefficient. Assuming an integral definition for effective stiffness $\bar{E} = \int_{-h/2}^{h/2} E(z, e_1)\, dz$, the tables suggest that the buckling load of fluid-free plates reduces by nearly identical rate as that of $\bar{E}$, when e_1 grows. For example, the critical buckling load for a simply supported fluid-free homogenous square plate with $h/a = 0.1$ under bilateral compressive loading, i.e. $R = 1$ decrease by 32.2% as the porosity coefficient adopts the value 0.5. The effective stiffness $\bar{E}$ drops by almost the same rate 31.8%, when e_1 rises from 0 to 0.5. A portion of this drop is compensated, when the pores are filled with a fluid. As the matter of fact, the entrapment of fluid in the interconnected network of pores causes the solid and fluid to behave as an integrated body,

sustaining the forces the applied to the boundaries in a more productive way with respect to the case in which the pores are free of fluid. For this reason, the buckling load of a fluid-saturated plate is higher comparing with the corresponding fluid-free plate. Although the influence of saturation condition on P_{cr} depends on various parameters including boundary and loading conditions, the overall increase generally varies around $2-6\%$, denoting that the major share of the load is being handled by the solid skeleton solely. To provide a deeper insight into the effect of pore fluid pressure on the stability of the system, the parameter θ, representing the relative difference in the critical buckling load of the fluid-saturated plate with respect the one free of fluid, is defined as:

$$\theta = \frac{P_{\mathrm{cr}}|_{B\neq 0} - P_{\mathrm{cr}}|_{B=0}}{P_{\mathrm{cr}}|_{B=0}} \times 100\,, \tag{33}$$

In Fig. 5, variation of θ against the pore pressure coefficient B is plotted for various boundary conditions for a plate subjected to different loading conditions. As mentioned above, an increment in P_{cr} is observed for all boundary conditions, and therewith positive θ. This indeed refers to the increasing equivalent stiffness of the plate as the result of increase in pore pressure. Furthermore, the rate of this grow depends on the type of constraints imposed on edges. Based on the figures, the curve corresponding to the simply supported plate lies above those of other boundary conditions, suggesting the greater effect of pore pressure coefficient on the plate under this specific boundary condition. Note that the curves associated to different boundary conditions becomes closer one another for the plate subjected to the first type of loading, i.e. $R=-1$. This perhaps stems from the influence of the applied tensile loading, as an external agent, on the increase in the pore pressure. Eventually, the final example of this section is shown in Fig. 6, where the effects of B on θ for a S-F-S-F porous plate with different values of porosity coefficient, namely 0.1, 0.25, 0.4, 0.55 and 0.7 is examined. One observes that the pore pressure coefficient B influence more effectively on plates with higher porosity coefficient. The underly reason for this trend could be attributed to the increase in the pore volume fraction inside the body, which subsequently leads to sustaining a greater portion of load by the fluid.

Table 4. The critical buckling load ($\times 10^{-4}$ *N/m*) for a rectangular plate with S-F-S-F boundary condition ($a = 1$)

e_1	Material	Theory	Aspect Ratio ($a/b = 0.5$)		Aspect Ratio ($a/b = 1$)	
			$h/a = 0.1$	$h/a = 0.2$	$h/a = 0.1$	$h/a = 0.2$
Plate subjected to biaxial compressive and tension loading ($R = -1$)						
0	Homogenous	FSDT	50.543	375.262	49.873	370.176
		TSDT	50.544	375.313	49.874	370.233
0.3	Fluid-free	FSDT	41.215	305.828	40.668	301.683
		TSDT	41.203	305.562	40.6580	301.426
	Fluid-saturated	FSDT	42.173	312.344	41.526	307.451
		TSDT	42.161	312.045	41.514	307.901
0.5	Fluid-free	FSDT	34.185	253.953	33.732	250.512
		TSDT	34.167	253.489	33.714	250.058
	Fluid-saturated	FSDT	35.591	263.524	34.995	259.027
		TSDT	35.578	262.983	34.974	258.502
0.7	Fluid-free	FSDT	25.983	193.918	25.639	191.290
		TSDT	25.987	193.340	25.617	190.723
	Fluid-saturated	FSDT	27.593	204.980	27.097	201.229
		TSDT	27.565	204.287	27.071	200.538
Plate subjected to uniaxial compressive loading ($R = 0$)						
0	Homogenous	FSDT	50.288	373.281	49.496	367.325
		TSDT	50.289	373.339	49.500	367.390
0.3	Fluid-free	FSDT	41.007	304.214	40.360	299.361
		TSDT	40.996	303.955	40.350	299.150
	Fluid-saturated	FSDT	41.918	310.381	41.155	304.680
		TSDT	41.906	310.093	41.144	304.409
0.5	Fluid-free	FSDT	34.013	252.613	33.477	248.582
		TSDT	33.995	252.156	33.460	248.140
	Fluid-saturated	FSDT	35.352	261.686	34.651	256.462
		TSDT	35.331	261.159	34.633	255.958
0.7	Fluid-free	FSDT	25.852	192.894	25.446	189.812
		TSDT	25.832	192.323	25.424	189.258
	Fluid-saturated	FSDT	27.391	203.421	26.810	199.071
		TSDT	27.364	202.729	26.784	198.407
Plate subjected to biaxial compressive loading ($R = +1$)						
0	Homogenous	FSDT	49.431	365.107	48.638	359.754
		TSDT	49.434	365.310	48.641	359.865
0.3	Fluid-free	FSDT	40.306	297.541	39.660	293.183
		TSDT	40.432	297.323	39.650	292.972
	Fluid-saturated	FSDT	41.433	302.134	40.313	297.321
		TSDT	41.036	302.050	40.304	297.096
0.5	Fluid-free	FSDT	33.433	247.092	32.897	243.464
		TSDT	33.416	247.600	32.880	243.050
	Fluid-saturated	FSDT	35.120	253.915	33.872	249.675
		TSDT	34.506	253.442	33.853	249.220
0.7	Fluid-free	FSDT	25.416	188.741	25.008	185.942
		TSDT	25.394	188.200	24.986	185.405
	Fluid-saturated	FSDT	27.424	196.875	26.161	193.433
		TSDT	26.665	198.100	26.136	192.854

Table 3: The critical buckling load ($\times 10^{-4}$ *N/m*) for a rectangular plate with S-S-S-S boundary condition ($a = 1$)

e_1	Material	Theory	Aspect Ratio ($a/b = 0.5$)		Aspect Ratio ($a/b = 1$)	
			$h/a = 0.1$	$h/a = 0.2$	$h/a = 0.1$	$h/a = 0.2$
Plate subjected to biaxial compressive and tension loading ($R = -1$)						
0	Homogenous	FSDT	106.169	775.276	387.638(*)	2299.031(*)
		TSDT	106.170	775.416	387.708(*)	2303.979(*)
0.3	Fluid-free	FSDT	86.570	631.722	315.861(*)	1869.851(*)
		TSDT	86.541	631.062	315.531(*)	1867.216(*)
	Fluid-saturated	FSDT	88.784	646.425	323.213(*)	1901.862(*)
		TSDT	88.752	645.681	322.840(*)	1898.756(*)
0.5	Fluid-free	FSDT	71.812	524.746	262.373(*)	1558.963(*)
		TSDT	71.765	523.586	261.793(*)	1551.427(*)
	Fluid-saturated	FSDT	75.048	546.257	273.129(*)	1605.933(*)
		TSDT	74.992	544.897	272.448(*)	1597.169(*)
0.7	Fluid-free	FSDT	54.603	401.252	200.626(*)	1210.676(*)
		TSDT	54.546	399.801	199.901(*)	1199.625(*)
	Fluid-saturated	FSDT	58.282	425.954	212.977(*)	1266.059(*)
		TSDT	58.212	424.162	212.081(*)	1252.723(*)
Plate subjected to uniaxial compressive loading ($R = 0$)						
0	Homogenous	FSDT	79.627	581.459	200.023	1391.442
		TSDT	79.628	581.562	200.029	1392.047
0.3	Fluid-free	FSDT	64.928	473.791	163.074	1133.264
		TSDT	64.906	473.297	162.992	1131.690
	Fluid-saturated	FSDT	66.588	484.819	167.163	1157.871
		TSDT	66.564	484.261	167.072	1156.091
0.5	Fluid-free	FSDT	53.859	393.559	135.313	942.235
		TSDT	53.824	392.689	135.178	939.285
	Fluid-saturated	FSDT	56.286	409.693	141.292	978.262
		TSDT	56.244	408.673	141.132	974.816
0.7	Fluid-free	FSDT	40.952	300.939	103.011	723.287
		TSDT	40.909	299.851	102.846	719.492
	Fluid-saturated	FSDT	43.712	319.465	109.823	764.934
		TSDT	43.659	318.121	109.618	760.276
Plate subjected to biaxial compressive loading ($R = +1$)						
0	Homogenous	FSDT	63.702	465.166	100.011	695.721
		TSDT	63.702	465.250	100.014	696.023
0.3	Fluid-free	FSDT	51.961	379.033	81.537	566.632
		TSDT	51.925	378.637	81.496	565.845
	Fluid-saturated	FSDT	53.264	387.855	83.582	578.936
		TSDT	53.251	387.409	83.535	578.045
0.5	Fluid-free	FSDT	43.116	314.848	67.657	471.117
		TSDT	43.059	314.151	67.588	469.642
	Fluid-saturated	FSDT	45.020	327.754	70.646	489.131
		TSDT	44.995	326.938	70.566	487.407
0.7	Fluid-free	FSDT	32.823	240.751	51.505	361.643
		TSDT	32.727	239.881	51.423	359.745
	Fluid-saturated	FSDT	34.994	255.572	54.912	382.467
		TSDT	34.927	254.497	54.809	380.137

Table 6. The critical buckling load ($\times 10^{-4}$ *N/m*) for a rectangular plate with S-C-S-C boundary condition ($a = 1$)

e_1	Material	Theory	Aspect Ratio ($a/b = 0.5$)		Aspect Ratio ($a/b = 1$)	
			$h/a = 0.1$	$h/a = 0.2$	$h/a = 0.1$	$h/a = 0.2$
Plate subjected to biaxial compressive and tension loading ($R = -1$)						
0	Homogenous	FSDT	133.917	928.097	464.048(*)	2525.305(*)
		TSDT	134.077	933.601	466.800(*)	2573.541(*)
0.3	Fluid-free	FSDT	109.175	755.916	377.958(*)	2052.854(*)
		TSDT	109.246	759.137	379.568(*)	2083.840(*)
	Fluid-saturated	FSDT	111.897	772.349	386.174(*)	2084.187(*)
		TSDT	111.968	775.639	387.819(*)	2115.674(*)
0.5	Fluid-free	FSDT	90.597	628.454	314.227(*)	1713.253(*)
		TSDT	90.607	630.089	315.044(*)	1732.426(*)
	Fluid-saturated	FSDT	94.576	652.514	326.257(*)	1759.292(*)
		TSDT	94.580	654.126	327.063(*)	1778.519(*)
0.7	Fluid-free	FSDT	68.992	482.312	241.156(*)	1336.270(*)
		TSDT	68.951	482.523	241.261(*)	1344.479(*)
	Fluid-saturated	FSDT	73.529	510.097	255.048(*)	1390.887(*)
		TSDT	73.471	510.083	255.041(*)	1398.061(*)
Plate subjected to uniaxial compressive loading ($R = 0$)						
0	Homogenous	FSDT	96.601	680.413	339.801(*)	1882.237(*)
		TSDT	96.472	681.242	340.621(*)	1902.521(*)
0.3	Fluid-free	FSDT	78.623	553.589	276.795(*)	1530.200(*)
		TSDT	78.615	554.051	277.026(*)	1540.593(*)
	Fluid-saturated	FSDT	80.601	565.857	282.929(*)	1553.936(*)
		TSDT	80.591	566.289	283.145(*)	1564.386(*)
0.5	Fluid-free	FSDT	65.235	460.133	230.066(*)	1276.887(*)
		TSDT	65.199	459.808	229.904(*)	1280.592(*)
	Fluid-saturated	FSDT	68.127	478.092	239.046(*)	1311.758(*)
		TSDT	68.083	477.638	238.819(*)	1315.059(*)
0.7	Fluid-free	FSDT	49.650	352.771	176.385(*)	995.315(*)
		TSDT	49.594	351.838	175.919(*)	993.189(*)
	Fluid-saturated	FSDT	52.944	373.483	186.742(*)	1036.674(*)
		TSDT	52.873	372.271	186.136(*)	1033.280(*)
Plate subjected to biaxial compressive loading ($R = +1$)						
0	Homogenous	FSDT	74.599	530.332	179.120	1085.083
		TSDT	74.608	530.789	179.215	1089.372
0.3	Fluid-free	FSDT	60.823	432.028	145.961	882.724
		TSDT	60.802	431.743	145.871	883.365
	Fluid-saturated	FSDT	62.360	441.715	149.379	898.357
		TSDT	62.336	441.375	149.274	898.880
0.5	Fluid-free	FSDT	50.755	359.042	121.231	735.623
		TSDT	50.424	358.280	121.023	733.8508
	Fluid-saturated	FSDT	52.734	373.221	126.232	758.563
		TSDT	52.664	372.315	125.985	756.3798
0.7	Fluid-free	FSDT	38.591	275.100	92.661	570.203
		TSDT	38.348	274.023	92.377	566.5484
	Fluid-saturated	FSDT	41.014	291.437	98.399	597.165
		TSDT	40.894	290.099	98.046	592.6504

Table 7: The critical buckling load ($\times 10^{-4}$ *N/m*) for a rectangular plate with S-S-S-C boundary condition ($a = 1$)

e_1	Material	Theory	Aspect Ratio ($a/b = 0.5$)		Aspect Ratio ($a/b = 1$)	
			$h/a = 0.1$	$h/a = 0.2$	$h/a = 0.1$	$h/a = 0.2$
Plate subjected to biaxial compressive and tension loading ($R = -1$)						
0	Homogenous	FSDT	118.349	844.765	422.383(*)	2407.278(*)
		TSDT	118.406	846.9825	423.491(*)	2431.200(*)
0.3	Fluid-free	FSDT	96.494	688.210	344.105(*)	1957.421(*)
		TSDT	96.499	689.037	344.518(*)	1969.496(*)
	Fluid-saturated	FSDT	98.935	703.755	351.877(*)	1989.192(*)
		TSDT	98.938	704.559	352.279(*)	2001.255(*)
0.5	Fluid-free	FSDT	80.057	571.890	285.945(*)	1632.754(*)
		TSDT	80.028	571.783	285.891(*)	1636.854(*)
	Fluid-saturated	FSDT	83.625	594.640	297.320(*)	1679.402(*)
		TSDT	83.589	594.403	297.201(*)	1682.881(*)
0.7	Fluid-free	FSDT	60.911	438.014	219.007(*)	1270.602(*)
		TSDT	60.858	437.167	218.583(*)	1267.853(*)
	Fluid-saturated	FSDT	64.974	464.206	232.103(*)	1325.769(*)
		TSDT	64.905	463.060	231.530(*)	1321.326(*)
Plate subjected to uniaxial compressive loading ($R = 0$)						
0	Homogenous	FSDT	86.755	624.342	276.589	1780.316
		TSDT	86.769	625.012	276.889	1791.870
0.3	Fluid-free	FSDT	70.737	508.669	225.435	1449.031
		TSDT	70.719	508.516	225.489	1454.766
	Fluid-saturated	FSDT	72.534	520.271	230.879	1477.181
		TSDT	72.514	520.067	230.924	1482.983
0.5	Fluid-free	FSDT	58.683	422.641	187.160	1206.350
		TSDT	58.647	421.955	187.048	1208.098
	Fluid-saturated	FSDT	61.310	439.620	195.122	1247.616
		TSDT	61.267	438.790	194.978	1249.126
0.7	Fluid-free	FSDT	44.638	323.531	142.798	931.137
		TSDT	44.589	322.480	142.565	929.442
	Fluid-saturated	FSDT	47.627	343.064	151.906	979.283
		TSDT	47.567	341.744	151.606	976.770
Plate subjected to biaxial compressive loading ($R = +1$)						
0	Homogenous	FSDT	68.053	491.861	129.712	852.442
		TSDT	68.055	492.070	129.743	854.051
0.3	Fluid-free	FSDT	55.488	400.747	105.731	693.931
		TSDT	55.469	400.381	105.674	693.560
	Fluid-saturated	FSDT	56.901	409.942	108.312	707.816
		TSDT	56.879	409.522	108.247	707.333
0.5	Fluid-free	FSDT	46.032	332.947	87.766	577.525
		TSDT	45.999	332.216	87.654	575.867
	Fluid-saturated	FSDT	48.096	346.402	91.541	597.872
		TSDT	48.058	345.540	91.408	595.899
0.7	Fluid-free	FSDT	35.010	254.791	66.920	445.155
		TSDT	34.970	253.836	66.775	442.580
	Fluid-saturated	FSDT	37.359	270.262	71.234	468.841
		TSDT	37.310	269.079	71.053	465.667

Table 8. The critical buckling load ($\times 10^{-4}$ *N/m*) for a rectangular plate with S-C-S-F boundary condition ($a = 1$)

e_1	Material	Theory	Aspect Ratio ($a/b = 0.5$)		Aspect Ratio ($a/b = 1$)	
			$h/a = 0.1$	$h/a = 0.2$	$h/a = 0.1$	$h/a = 0.2$
Plate subjected to biaxial compressive and tension loading ($R = -1$)						
0	Homogenous	FSDT	62.394	458.552	124.737	864.930
		TSDT	62.469	458.846	124.922	869.720
0.3	Fluid-free	FSDT	50.876	373.672	101.691	704.480
		TSDT	50.866	373.642	101.913	707.216
	Fluid-saturated	FSDT	52.031	381.362	103.679	716.045
		TSDT	52.019	381.149	103.736	718.919
0.5	Fluid-free	FSDT	42.202	310.348	84.387	585.672
		TSDT	42.199	309.868	84.389	586.985
	Fluid-saturated	FSDT	43.899	321.662	87.333	602.883
		TSDT	43.872	321.091	88.765	604.147
0.7	Fluid-free	FSDT	32.085	237.165	64.265	449.419
		TSDT	32.064	236.490	64.222	449.469
	Fluid-saturated	FSDT	34.032	250.289	67.699	469.851
		TSDT	33.997	249.449	67.639	469.666
Plate subjected to uniaxial compressive loading ($R = 0$)						
0	Homogenous	FSDT	57.566	423.711	84.573	599.982
		TSDT	57.569	423.879	84.606	601.172
0.3	Fluid-free	FSDT	46.940	345.286	68.953	488.777
		TSDT	46.928	345.043	68.975	489.029
	Fluid-saturated	FSDT	47.929	351.854	69.999	495.113
		TSDT	47.917	351.728	69.992	495.339
0.5	Fluid-free	FSDT	38.936	286.763	57.211	406.188
		TSDT	38.915	286.261	57.180	406.110
	Fluid-saturated	FSDT	40.394	296.458	58.789	415.800
		TSDT	40.369	295.876	58.997	415.405
0.7	Fluid-free	FSDT	29.601	219.110	43.543	311.179
		TSDT	29.598	218.448	43.497	310.342
	Fluid-saturated	FSDT	31.284	230.429	45.434	322.906
		TSDT	31.251	229.628	45.376	321.895
Plate subjected to biaxial compressive loading ($R = +1$)						
0	Homogenous	FSDT	51.984	380.079	58.851	417.601
		TSDT	51.991	381.311	58.869	418.053
0.3	Fluid-free	FSDT	42.387	309.715	47.980	340.211
		TSDT	42.377	310.366	47.971	340.086
	Fluid-saturated	FSDT	43.040	313.552	48.401	342.492
		TSDT	43.037	316.666	48.391	342.362
0.5	Fluid-free	FSDT	35.162	257.246	39.811	282.707
		TSDT	35.145	257.500	39.785	282.212
	Fluid-saturated	FSDT	36.138	263.057	40.486	286.481
		TSDT	36.241	264.074	40.458	285.959
0.7	Fluid-free	FSDT	26.739	196.639	30.305	216.525
		TSDT	26.713	196.415	30.267	215.780
	Fluid-saturated	FSDT	27.902	203.774	31.185	221.670
		TSDT	27.955	203.082	31.142	220.859

Table 9: The critical buckling load ($\times 10^{-4}$ *N/m*) for a rectangular plate with S-S-S-F boundary condition ($a = 1$)

e_1	Material	Theory	Aspect Ratio ($a/b = 0.5$)		Aspect Ratio ($a/b = 1$)	
			$h/a = 0.1$	$h/a = 0.2$	$h/a = 0.1$	$h/a = 0.2$
Plate subjected to biaxial compressive and tension loading ($R = -1$)						
0	Homogenous	FSDT	60.461	446.884	99.806	727.202
		TSDT	60.462	446.954	99.810	728.642
0.3	Fluid-free	FSDT	49.301	364.182	81.380	592.545
		TSDT	49.320	363.852	81.369	591.968
	Fluid-saturated	FSDT	50.435	371.807	83.023	603.102
		TSDT	50.419	371.450	83.013	602.454
0.5	Fluid-free	FSDT	40.894	302.436	67.509	492.211
		TSDT	40.871	301.875	67.468	491.975
	Fluid-saturated	FSDT	42.557	313.648	69.940	507.883
		TSDT	42.530	312.972	71.234	506.656
0.7	Fluid-free	FSDT	31.085	231.022	51.336	376.404
		TSDT	31.058	230.298	51.282	375.062
	Fluid-saturated	FSDT	32.993	244.007	54.159	394.860
		TSDT	32.958	243.119	54.093	393.364
Plate subjected to uniaxial compressive loading ($R = 0$)						
0	Homogenous	FSDT	56.222	415.432	72.520	528.705
		TSDT	56.224	415.510	72.526	528.882
0.3	Fluid-free	FSDT	45.845	338.552	59.131	430.812
		TSDT	45.832	338.255	59.115	430.437
	Fluid-saturated	FSDT	46.835	345.169	60.133	437.199
		TSDT	46.821	344.840	60.116	436.789
0.5	Fluid-free	FSDT	38.027	281.151	49.053	357.850
		TSDT	38.006	280.620	49.023	357.127
	Fluid-saturated	FSDT	39.483	290.905	50.551	367.448
		TSDT	39.459	290.370	50.516	366.634
0.7	Fluid-free	FSDT	28.907	214.761	37.304	273.613
		TSDT	28.881	214.096	37.266	272.822
	Fluid-saturated	FSDT	30.585	226.120	39.074	285.137
		TSDT	30.553	225.316	39.029	284.042
Plate subjected to biaxial compressive loading ($R = +1$)						
0	Homogenous	FSDT	51.482	377.518	54.694	394.752
		TSDT	51.512	378.024	54.704	395.036
0.3	Fluid-free	FSDT	41.978	307.635	44.594	321.639
		TSDT	41.968	310.229	44.938	321.460
	Fluid-saturated	FSDT	42.665	311.701	45.095	324.448
		TSDT	42.883	311.479	45.085	324.336
0.5	Fluid-free	FSDT	34.822	255.507	36.997	267.203
		TSDT	34.803	255.308	36.974	266.724
	Fluid-saturated	FSDT	35.844	261.622	37.774	271.659
		TSDT	36.241	261.130	37.749	271.196
0.7	Fluid-free	FSDT	26.477	195.272	28.146	204.425
		TSDT	26.452	196.287	28.115	203.754
	Fluid-saturated	FSDT	27.686	202.710	29.117	210.215
		TSDT	27.681	202.716	29.081	209.564

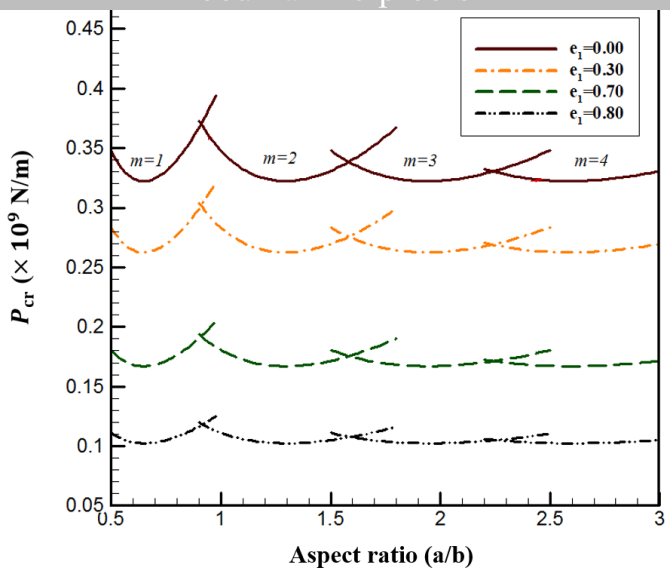

Fig. 4: Effect of aspect ratio on the critical buckling mode of a SCSC porous plate ($h/b = 0.1$, $R = 0$)

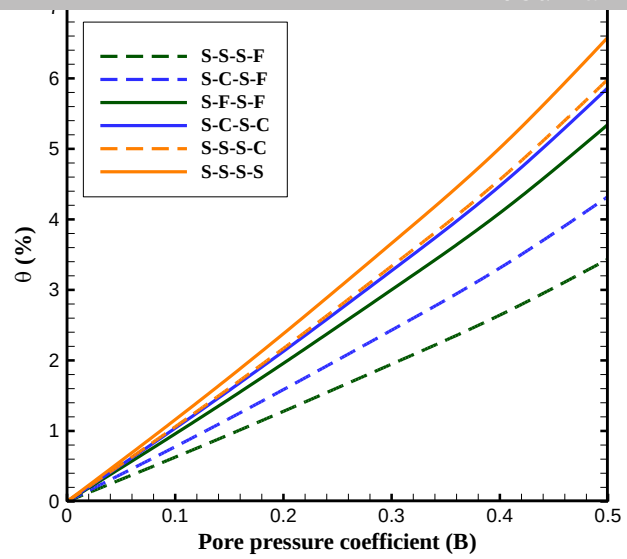

(a)

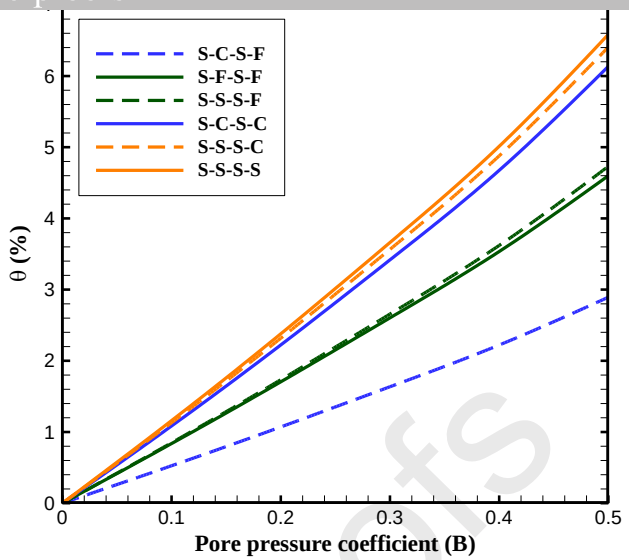

(b)

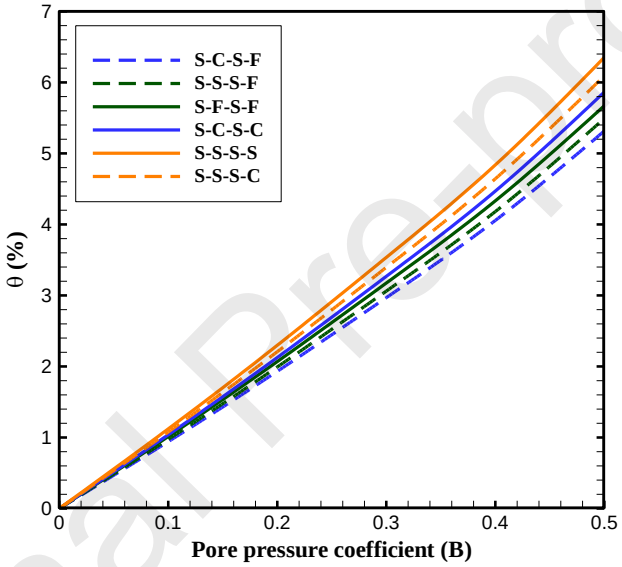

(c)

Fig. 5: Effect of pore pressure coefficient on the critical buckling load of a porous plate: a) $R = 0$, b) $R = 1$, and c) $R = -1$ ($a/b = 1$, $h/a = 0.1$, $e_1 = 0.7$)

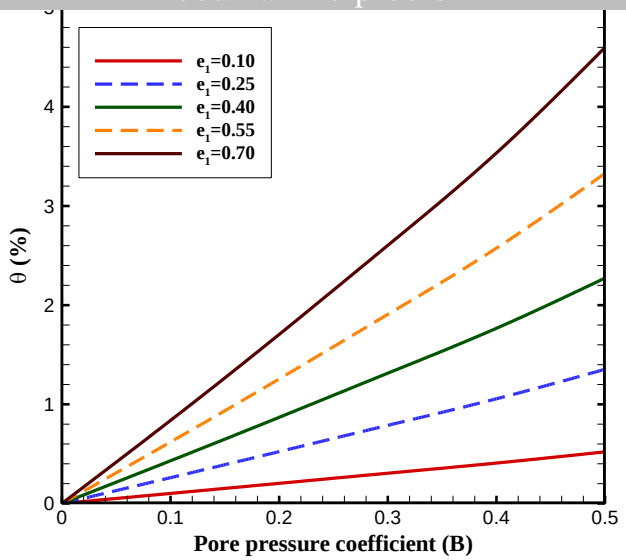

Fig. 6: Effect of pore pressure coefficient on the critical buckling load of a S-F-S-F porous plate with different porosity coefficients ($a/b = 1$, $h/a = 0.1$, $R = 1$)

6. Concluding remarks

Buckling analysis of a rectangular porous plate constrained by Levy-type boundary conditions and subjected to in-plane compressional/tensile loading was carried out in this study. Different states regarding the saturation of internal pores were considered based on Biot's poroelasticity theory. The porosity is assumed to vary along the thickness following a well-known cosine rule. Both first-order and third-order shear deformation theories were employed to realize the safe threshold for use of each theory while studying buckling problems. The critical buckling loads of the system were computed based on an analytical solution, reached by applying an efficient decoupling procedure to the governing equations of motion. A comprehensive parametric study was performed to highlight the effect of different parameters involved including saturation, loading and boundary conditions on the response. Major findings are listed as follows:

- The results imply that both theories would yield plausible response if used in the proper range of thickness.
- It is revealed that the increase in pore volume fraction is accompanied by a decrease in the critical buckling load.
- Increasing pore pressure coefficient leads to higher critical buckling loads.
- Sensitivity of the buckling load growth, as the consequence of increasing pore fluid compressibility, to various parameters including the loading and boundary conditions is demonstrated.

Funding
The authors received no financial support for the research, authorship, and/or publication of this article.

Appendix A:

$$\begin{pmatrix}\tilde{a}_{22}\\ \tilde{b}_{11}\\ \tilde{b}_{22}\\ \tilde{c}_{11}\\ \tilde{c}_{22}\\ \tilde{h}_{11}\end{pmatrix}=\begin{pmatrix}a_{22}\\ b_{11}\\ b_{22}\\ c_{11}\\ c_{22}\\ 0\end{pmatrix}-\eta\begin{pmatrix}6c_{22}\\ d_{11}\\ d_{22}\\ 2f_{11}\\ 2f_{22}\\ f_{11}\end{pmatrix}+\eta^2\begin{pmatrix}9f_{22}\\ 0\\ 0\\ h_{11}\\ h_{22}\\ -h_{11}\end{pmatrix} \tag{A.1}$$

And

$$\begin{pmatrix}\hat{c}_{11}\\ \hat{b}_{11}\\ \hat{h}_{11}\\ \hat{f}_{11}\\ \hat{a}_{11}\end{pmatrix}=\begin{pmatrix}\tilde{c}_{11}\\ \tilde{c}_{22}\\ \tilde{h}_{11}\\ \eta^2 h_{11}\\ \tilde{a}_{22}\end{pmatrix}-\frac{1}{a_{11}}\begin{pmatrix}(\tilde{b}_{11})^2\\ \tilde{b}_{11}\tilde{b}_{22}\\ \eta\tilde{b}_{11}d_{11}\\ (\eta d_{11})^2\\ 0\end{pmatrix} \tag{A.2}$$

And

$$\begin{pmatrix}\bar{c}_{11}\\ \bar{d}_{11}\end{pmatrix}=\begin{pmatrix}\dfrac{\hat{f}_{11}\hat{c}_{11}-\hat{h}_{11}\hat{h}_{11}}{\hat{a}_{11}}\\ c_{11}-\dfrac{b_{11}^2}{a_{11}}\end{pmatrix} \tag{A.3}$$

References

[1] Theodorakopoulos DD, Beskos DE. Flexural vibrations of poroelastic plates. Acta Mechanica 1994;103:191–203. https://doi.org/10.1007/BF01180226.

[2] Leclaire P, Horoshenkov K v., Cummings A. Transverse vibrations of a thin rectangular porous plate saturated by a fluid. Journal of Sound and Vibration 2001;247:1–18. https://doi.org/10.1006/jsvi.2001.3656.

[3] Leclaire P, Horoshenkov K v., Swift MJ, Hothersall DC. The vibrational response of a clamped rectangular porous plate. Journal of Sound and Vibration 2001;247:19–31. https://doi.org/10.1006/jsvi.2000.3657.

[4] Aygun H, Attenborough K, Cummings A. Predicted effects of fluid loading on the vibration of elastic porous plates. Acta Acustica United with Acustica 2007;93:284–9.

[5] Rezaei AS, Saidi AR. Exact solution for free vibration of thick rectangular plates made of porous materials. Composite Structures 2015;134:1051–60. https://doi.org/10.1016/j.compstruct.2015.08.125.

[6] Rezaei AS, Saidi AR. Application of Carrera Unified Formulation to study the effect of porosity on natural frequencies of thick porous-cellular plates. Composites Part B: Engineering 2016;91:361–70. https://doi.org/10.1016/j.compositesb.2015.12.050.

[7] Akbaş ŞD. Forced vibration analysis of functionally graded porous deep beams. Composite Structures 2018;186:293–302. https://doi.org/10.1016/j.compstruct.2017.12.013.

[8] Shahsavari D, Shahsavari M, Li L, Karami B. A novel quasi-3D hyperbolic theory for free vibration of FG plates with porosities resting on Winkler/Pasternak/Kerr foundation. Aerospace Science and Technology 2018;72:134–49. https://doi.org/10.1016/j.ast.2017.11.004.

[9] Askari M, Saidi AR, Rezaei AS. On natural frequencies of Levy-type thick porous-cellular plates surrounded by piezoelectric layers. Composite Structures 2017;179:340–54. https://doi.org/10.1016/j.compstruct.2017.07.073.

[10] Wang YQ, Zu JW. Porosity-dependent nonlinear forced vibration analysis of functionally graded piezoelectric smart material plates Related content Porosity-dependent nonlinear forced vibration analysis of functionally graded piezoelectric smart material plates. Smart Mater Struct 2017;26:105014. https://doi.org/10.1088/1361-665X/aa8429.

[11] Arshid E, Khorshidvand AR. Free vibration analysis of saturated porous FG circular plates integrated with piezoelectric actuators via differential quadrature method. Thin-Walled Structures 2018;125:220–33. https://doi.org/10.1016/j.tws.2018.01.007.

[12] Barati MR, Zenkour AM. Electro-thermoelastic vibration of plates made of porous functionally graded piezoelectric materials under various boundary conditions. Journal of Vibration and Control 2018;24:1910–26. https://doi.org/10.1177/1077546316672788.

[13] Biot MA. Theory of buckling of a porous slab and its thermoelastic analogy. Journal of Applied Mechanics, Transactions ASME 1964;31:194–8. https://doi.org/10.1115/1.3629586.

[14] Magnucki K, Malinowski M, Kasprzak J. Bending and buckling of a rectangular porous plate. Steel and Composite Structures 2006;6:319–33. https://doi.org/10.12989/scs.2006.6.4.319.

[15] Magnucka-Blandzi E. Axi-symmetrical deflection and buckling of circular porous-cellular plate. Thin-Walled Structures 2008;46:333–7. https://doi.org/10.1016/j.tws.2007.06.006.

[16] Jabbari M, Mojahedin A, Haghi M. Buckling analysis of thin circular FG plates made of saturated porous-soft ferromagnetic materials in transverse magnetic field. Thin-Walled Structures 2014;85:50–6. https://doi.org/10.1016/j.tws.2014.07.018.

[17] Chen D, Yang J, Kitipornchai S. Elastic buckling and static bending of shear deformable functionally graded porous beam. Composite Structures 2015;133:54–61. https://doi.org/10.1016/j.compstruct.2015.07.052.

[18] Chen D, Yang J, Kitipornchai S. Free and forced vibrations of shear deformable functionally graded porous beams. International Journal of Mechanical Sciences 2016;108–109:14–22. https://doi.org/10.1016/j.ijmecsci.2016.01.025.

[19] Rezaei AS, Saidi AR. Buckling response of moderately thick fluid-infiltrated porous annular sector plates. Acta Mechanica 2017;228:3929–45. https://doi.org/10.1007/s00707-017-1908-2.

[20] Dong YH, Li YH, Chen D, Yang J. Vibration characteristics of functionally graded graphene reinforced porous nanocomposite cylindrical shells with spinning motion. Composites Part B: Engineering 2018;145:1–13. https://doi.org/10.1016/j.compositesb.2018.03.009.

[21] Kamranfard M, Saidi A, Naderi A. Analytical solution for vibration and buckling of annular sectorial porous plates under in-plane uniform compressive loading. Proceedings of the Institution of Mechanical Engineers, Part C: Journal of Mechanical Engineering Science 2018;232:2211–28. https://doi.org/10.1177/0954406217716197.

[22] Tang H, Li L, Hu Y. Buckling analysis of two-directionally porous beam. Aerospace Science and Technology 2018;78:471–9. https://doi.org/10.1016/j.ast.2018.04.045.

[23] Merdaci S, Belghoul H. High-order shear theory for static analysis of functionally graded plates with porosities. Comptes Rendus - Mecanique 2019;347:207–17. https://doi.org/10.1016/j.crme.2019.01.001.

[24] Barati MR, Sadr MH, Zenkour AM. Buckling analysis of higher order graded smart piezoelectric plates with porosities resting on elastic foundation. International Journal of Mechanical Sciences 2016;117:309–20. https://doi.org/10.1016/j.ijmecsci.2016.09.012.

[25] Barati MR, Zenkour AM. Post-buckling analysis of refined shear deformable graphene platelet reinforced beams with porosities and geometrical imperfection. Composite Structures 2017;181:194–202. https://doi.org/10.1016/j.compstruct.2017.08.082.

[26] Barati MR, Zenkour AM. Investigating post-buckling of geometrically imperfect metal foam nanobeams with symmetric and asymmetric porosity distributions. Composite Structures 2017;182:91–8. https://doi.org/10.1016/j.compstruct.2017.09.008.

[27] Sobhy M, Zenkour AM. Porosity and inhomogeneity effects on the buckling and vibration of double-FGM nanoplates via a quasi-3D refined theory. Composite Structures 2019;220:289–303. https://doi.org/10.1016/j.compstruct.2019.03.096.

[28] Barati MR, Zenkour AM. Analysis of postbuckling of graded porous GPL-reinforced beams with geometrical imperfection. Mechanics of Advanced Materials and Structures 2019;26:503–11. https://doi.org/10.1080/15376494.2017.1400622.

[29] Daikh AA, Zenkour AM. Free vibration and buckling of porous power-law and sigmoid functionally graded sandwich plates using a simple higher-order shear deformation theory. Mater Res Express 2019;6:115707. https://doi.org/10.1088/2053-1591/ab48a9.

[30] Cong PH, Chien TM, Khoa ND, Duc ND. Nonlinear thermomechanical buckling and post-buckling response of porous FGM plates using Reddy's HSDT. Aerospace Science and Technology 2018;77:419–28. https://doi.org/10.1016/j.ast.2018.03.020.

[31] Tu TM, Hoa LK, Hung DX, Hai LT. Nonlinear buckling and post-buckling analysis of imperfect porous plates under mechanical loads. Journal of Sandwich Structures & Materials 2018:109963621878961. https://doi.org/10.1177/1099636218789612.

[32] Ibnorachid Z, Boutahar L, el Bikri K, Benamar R. Buckling temperature and natural frequencies of thick porous functionally graded beams resting on elastic foundation in a

thermal environment. Advances in Acoustics and Vibration 2019;2019. https://doi.org/10.1155/2019/7986569.

[33] Radwan AF. Quasi-3D integral model for thermomechanical buckling and vibration of FG porous nanoplates embedded in an elastic medium. International Journal of Mechanical Sciences 2019;157–158:320–35. https://doi.org/10.1016/j.ijmecsci.2019.04.031.

[34] Zenkour AM, Aljadani MH. Porosity effect on thermal buckling behavior of actuated functionally graded piezoelectric nanoplates. European Journal of Mechanics, A/Solids 2019;78:103835. https://doi.org/10.1016/j.euromechsol.2019.103835.

[35] Askari M, Brusa E, Delprete C. Electromechanical Vibration Characteristics of Porous Bimorph and Unimorph Doubly Curved Panels. Actuators 2020;9:7. https://doi.org/10.3390/act9010007.

[36] Askari M, Saidi A, Rezaei A. An investigation over the effect of piezoelectricity and porosity distribution on natural frequencies of porous smart plates. Journal of Sandwich Structures & Materials 2018:109963621879109. https://doi.org/10.1177/1099636218791092.

[37] Rezaei A, Saidi A. An analytical study on the free vibration of moderately thick fluid-infiltrated porous annular sector plates. Journal of Vibration and Control 2018;24:4130–44. https://doi.org/10.1177/1077546317721416.

[38] Wang YQ, Ye C, Zu JW. Vibration analysis of circular cylindrical shells made of metal foams under various boundary conditions. International Journal of Mechanics and Materials in Design 2019;15:333–44. https://doi.org/10.1007/s10999-018-9415-8.

[39] Wang YQ, Zhao HL. Bending, buckling and vibration of shear deformable beams made of three-dimensional graphene foam material. Journal of the Brazilian Society of Mechanical Sciences and Engineering 2019;41:1–17. https://doi.org/10.1007/s40430-019-1926-1.

[40] Detournay E, Cheng AHD. Fundamentals of poroelasticity. Comprehensive Rock Engineering Vol 2 1993:113–71. https://doi.org/10.1016/b978-0-08-040615-2.50011-3.

[41] Sharifan MH, Jabbari M. Mechanical Buckling Analysis of Saturated Porous Functionally Graded Elliptical Plates Subjected to In-Plane Force Resting on Two Parameters Elastic Foundation Based on HSDT. Journal of Pressure Vessel Technology, Transactions of the ASME 2020;142. https://doi.org/10.1115/1.4046707.

[42] Skempton AW. The Pore-Pressure Coefficient in Saturated Soils. Géotechnique 1960;10:186–7. https://doi.org/10.1680/geot.1960.10.4.186.

[43] Reddy JN. Mechanics of laminated composite plates and shells: theory and analysis. CRC Press; 2003.

[44] Brush DO, Almroth BO, Hutchinson JW. Buckling of Bars, Plates, and Shells. Journal of Applied Mechanics 1975;42:911–911. https://doi.org/10.1115/1.3423755.

[45] Shufrin I, Eisenberger M. Stability and vibration of shear deformable plates - First order and higher order analyses. International Journal of Solids and Structures 2005;42:1225–51. https://doi.org/10.1016/j.ijsolstr.2004.06.067.

[46] Hosseini-Hashemi S, Khorshidi K, Amabili M. Exact solution for linear buckling of rectangular Mindlin plates. Journal of Sound and Vibration 2008;315:318–42. https://doi.org/10.1016/j.jsv.2008.01.059.

Author statement

E. Sadeghi Rad: Conceptualization, Methodology, Formal analysis, Investigations, Validation, Software.

A. R. Saidi: Conceptualization, Supervision.

A. S. Rezaei: Conceptualization, Methodology, Writing - Original Draft.

M. Askari*:* Validation, Software, Writing - Original Draft, Writing - Review & Editing.